Current Research in Biotechnology 9 (2025) 100298

Contents lists available at ScienceDirect

Current Research in Biotechnology

journal homepage: www.elsevier.com/locate/crbiot

Neurotensin(8-13) analogs targeting NTS1 and NTS2 receptors: A comparative *in vitro* and molecular modeling study☆

Kiril Kirilov [a], Maria Ponticelli [a,b], Toni Kühl [c], Harald Hübner [d], Maya G. Georgieva [a], Matthias Vogel [e], Aneliya A. Balacheva [a], Bodo Haas [e], Tamara I. Pajpanova [a], Maima Matin [f], Luigi Milella [b], Peter Gmeiner [d], Diana Imhof [c], Nikolay T. Tzvetkov [a,*]

[a] *Department of Biochemical Pharmacology and Drug Design, Institute of Molecular Biology "Roumen Tsanev", Bulgarian Academy of Sciences, Acad. G. Bonchev Str., bl. 21, Sofia 1113, Bulgaria*
[b] *Department of Science, University of Basilicata, V.le ell'Ateneo Lucano 10, 85100 Potenza, Italy*
[c] *Pharmaceutical Biochemistry and Bioanalytics, Pharmaceutical Institute, University of Bonn, An der Immenburg 4, D-53121 Bonn, Germany*
[d] *Department of Chemistry and Pharmacy, Medicinal Chemistry, Friedrich-Alexander- Universität Erlangen-Nürnberg, Nikolaus-Fiebiger-Str. 10, D-91058 Erlangen, Germany*
[e] *Federal Institute for Drugs and Medical Devices (BfArM), Kurt-Georg-Kiesinger-Allee 3, 53175 Bonn, Germany*
[f] *Institute of Genetics and Animal Biotechnology of the Polish Academy of Sciences, Jastrzebiec, 05-552 Magdalenka, Poland*

ARTICLE INFO

Keywords:
In vitro studies
Neurotensin
Neurotensin receptors
Molecular Modeling
MD simulation

ABSTRACT

The simultaneous activation of both neurotensin type 1 and 2 receptors (NTS1R and NTS2R) through the neuronal peptide neurotensin (NT), activating the dopamine (DA) release and DA signaling within the dopaminergic system in the brain, suggest that NTS1R/NTS2R dual-specific NT analogs may represent an attractive tool in the treatment of Parkinson's disease (PD) and/or other related conditions. Herein, we report *in silico* exploration of NTS1R and NTS2R driven by *in vitro* pharmacological evaluation of the linear hexapeptide NT analogs **3** (sequence Lys^{8}-Cav^{9}-Pro^{10}-Tyr^{11}-Ile^{12}-Leu^{13}) and **6** (Arg^{8}-Cav^{9}-Pro^{10}-Tyr^{11}-Ile^{12}-Leu^{13}), both active towards the human NTS1R and NTS2R. Compared to the parent peptide NT(8–13) (**2**), compounds **3** and **6** showed improved *in vitro* human plasma stability and BBB permeability. Moreover, *in silico* ADMET evaluation indicated that both NT-analogs have strong pharmacological properties combined with good safety profiles, highlighting their potential for further structural improvements. Furthermore, we applied an AI-based approach to generate the homology models of hNTS1R and hNTS2R, followed by MD simulations of their ligand-free state and molecular docking in order to estimate the most probable protein–ligand complexes of peptides **3** and **6**. Binding interaction/affinity analysis of the best-ranked docking modes, obtained with selected time-frames from the respective MD trajectories, suggest that the receptor activation occurs via a ligand-receptor binding into the initial "entry" conformation of hNTS1R and hNTS2R. This assumption is supported by additional HYDE analysis confirming the binding affinities of peptides **3** and **6** towards hNTS1R and hNTS2R obtained by radioligand binding experiments. The reported study may serve as a ready-to-use *in silico* approach for further development of therapeutic options against PD and potentially other neurological disorders.

Abbreviations: ADMET, absorption, distribution, metabolism, excretion, and toxicity; AI, artificial intelligence; BBB, blood–brain barrier; CNS, central nervous system; DA, dopamine; Fmoc, N-(9-fluorenyl)-methoxycarbonyl; DMSO, *N*,*N*-dimethyl sulfoxide; EM, energy minimization; GIT, gastrointestinal tract; GPCR, G protein-coupled receptor; HLM, human liver microsomes; IL, initial latency; LC-MS, liquid chromatography mass spectrometry; LLE, ligand-lipophilicity efficiency; MD, molecular dynamics; MW, molecular weight; NT, neurotensin; NT(8–13), neurotensin sequence 8–13; NTSRs, neurotensin receptors; NTS1R, neurotensin type 1 receptor; NTS2R, neurotensin type 2 receptor; nHA, number hydrogen acceptors; nHD, number of hydrogen donors; nRot, number of rotatable bonds; nRong, number of rings; 6-OHDA, 6-hydroxydopamine; PAMPA, parallel artificial membrane permeability assay; PBS, phosphate-buffered saline; PD, Parkinsońs disease; PPB, plasma protein binding; RP-HPLC, reversed-phase high-performance liquid chromatography; SN, substantia nigra; SPPS, solid-phase peptide synthesis; TFA, trifluoroacetic acid; TLC, thin layer chromatography; *t*PSA, topological polar surface area; VdW, Van der Waals; Vps10p, vacuolar protein sorting 10 protein; VTA, ventral tegmental area.

☆ This article is part of a special issue entitled: '10th Bulgarian PS' published in Current Research in Biotechnology.

* Corresponding author.
E-mail address: ntzvetkov@bio21.bas.bg (N.T. Tzvetkov).

https://doi.org/10.1016/j.crbiot.2025.100298
Received 16 February 2025; Received in revised form 19 April 2025; Accepted 6 May 2025
Available online 14 May 2025

1. Introduction

Parkinson's disease (PD) is one of the most prevalent age-dependent neurodegenerative disease of the central nervous system (CNS) affecting about 3 % of the population over age 65 worldwide (Dawson and Dawson, 2019; Romero-Zerbo et al., 2024; Videira and Castro-Caldas, 2018). The disease is typically characterized by a progressive degradation and loss of dopaminergic (DAergic) neurons in the *substantia nigra pars compacta* (SNc) of the midbrain (nigrostriatal pathway), leading to irreversible motor disturbances with clinical symptoms such as rigidity, resting tremor, bradykinesia (slowness), and postural instability (Tzvetkov et al., 2019; Naoi et al., 2024; Kakkar and Dahiya, 2015; Aarsland et al., 2017; Zigmond and Smeyne, 2014). Along with motor symptoms, there are also other neurological changes including behavioral and cognitive complications causing several non-motor symptoms like hyposmia, depression, anxiety, sleep disturbances, apathy, hallucinations, and dementia (Videira and Castro-Caldas, 2018; Tzvetkov et al., 2019). The DAergic degeneration is triggered by complex pathophysiological processes including oxidative stress and the associated thereof abnormal α-synuclein folding and accumulation, mitochondrial dysfunction, proteasome dysregulation, and neuroinflammation, along with others (Dawson and Dawson, 2019; Romero-Zerbo et al., 2024; Videira and Castro-Caldas, 2018; Tzvetkov et al., 2019). Despite enormous research efforts, the current management of PD involve therapeutic applications focused on elevation of the DA levels at different stages of the disease progression, but the disease still remains uncurable.

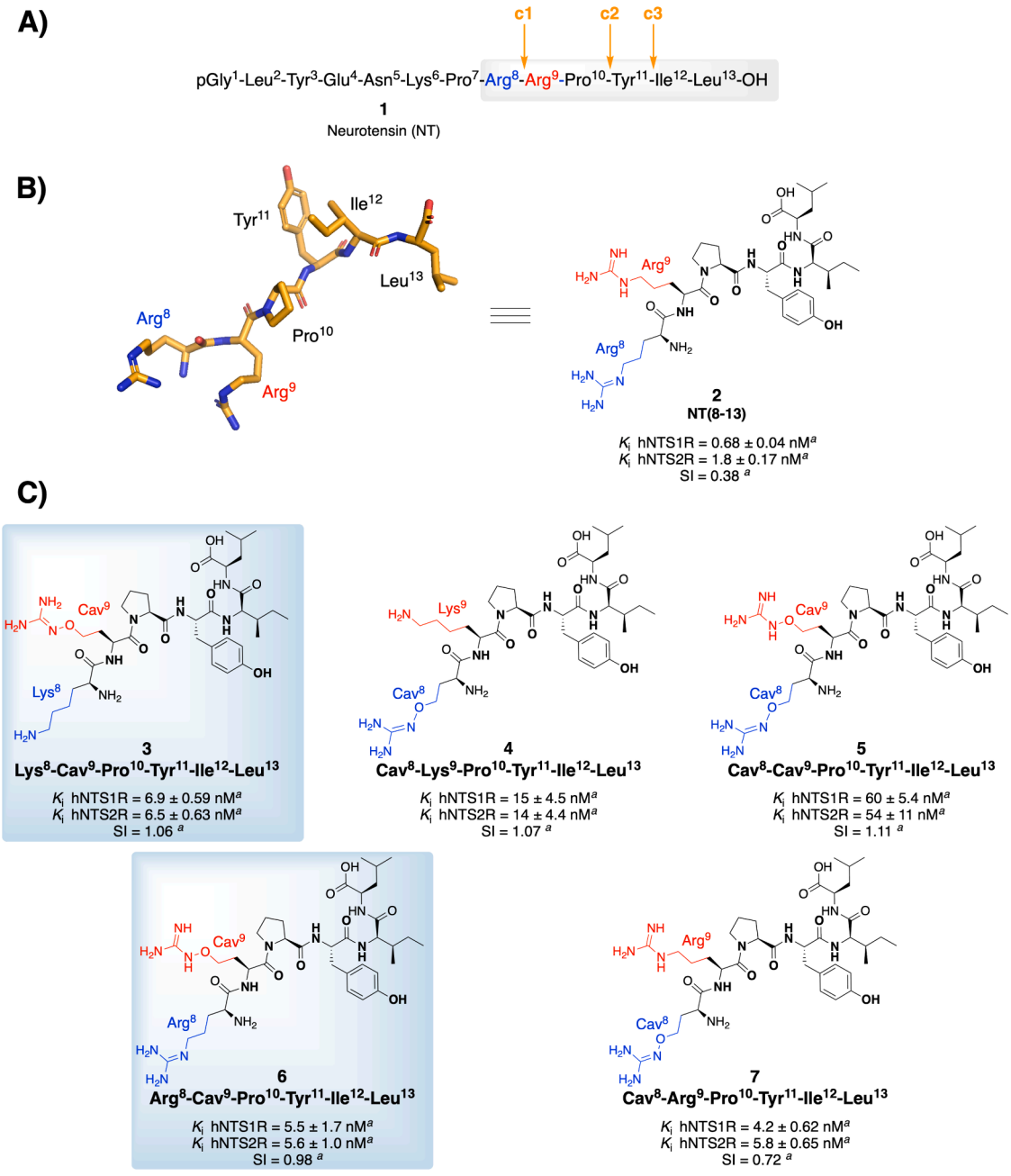

Fig. 1. A) Amino acid sequence of NT (1) with its major peptidase cleavage sites (c1–c3, in orange). B) 3D conformation and chemical structure of the biologically active fragment NT(8–13) (2). C) Chemical structures of linear NT(8–13) analogs 3–7 with the introduced substitutions at positions 8 (in blue) and 9 (in red). [a] The reported binding affinities and selectivity indexes (SIs) are from Ref. (Kühl et al., 2023). (For interpretation of the references to color in this figure legend, the reader is referred to the web version of this article.)

Thus, there is a medical need of PD-modifying therapeutic approaches.

The endogenous tridecapeptide neurotensin (NT), which possesses the sequence pELYENKPRRPYIL-OH, pE: pyroGlu (for structures, see Fig. 1), is widely expressed in the CNS where NT acts as a neurotransmitter or neuromodulator via interaction with DAergic, glutamatergic, GABAergic, cholinergic, and serotonergic systems (Yeung et al., 2020; Iyer and Kunos, 2021; Woodworth et al., 2018; Boules et al., 2013; Sarret and Cavelier, 2017; Tanganelli et al., 2012; Plach et al., 2019). In the periphery, NT acts mainly in the gastrointestinal tract (GIT) as a paracrine-endocrine hormone (Yeung et al., 2020; Vincent et al., 1999; Chartier et al., 2021). In general, NT exerts its physiological functions in the brain and in peripheral organs by interacting with two G protein-coupled receptors (GPCRs), the NT receptor type 1 and 2 (NTS1R and NTS2R), with higher affinity of NT against NTS1R over NTS2R (Yeung et al., 2020; Boules et al., 2013; Sousbie et al., 2018). NT is also an endogenous ligand of the single transmembrane domain intracellular sorting protein NTS3R/sortilin/gp95 (type I membrane glycoprotein Vps10p family sorting receptors) and NTS4R/SorLA/LR11 (yeast sorting sortilin related receptor), for which the mediating role of NT is still not fully understood (Yeung et al., 2020; Sousbie et al., 2018; Jacobsen et al., 2001; Li et al., 2005; Kleczkowska and Lipkowski, 2013). In the CNS, NT exerts its functions via activation of both NTS1 and NTS2 receptors, while in the gut it activates only NTS1R (Yeung et al., 2020; Sousbie et al., 2018). Therefore, NT possesses a variety of biological effects and is involved in the regulation of key physiological processes within the brain and the gut including non-opioid analgesia, regulation of neurotransmitter signaling, hypothermia, hypotension, and others (Yeung et al., 2020; Iyer and Kunos, 2021; Sousbie et al., 2018).

NT is highly expressed in the amygdala, lateral septum, ventral tegmental area (VTA), and substantia nigra (SN), where its neurophysiological effects are associated with directly antagonistic (e.g., NT/D_2 receptor interaction) or indirectly (e.g., second messenger-dependent receptor alteration) modulation of dopamine (DA) neurotransmission (Boules et al., 2013; Tanganelli et al., 2012; St-Gelais et al., 2004). In addition, the NTS1R is co-localized within the nigrostriatal pathway with both presynaptic and postsynaptic dopamine D_2 receptors (NTS1R–D_2R) (Plach et al., 2019; Mustain et al., 2011). Thus, such allosteric NTS1R–D_2R interaction leads to an increase in DA levels via NT-mediated inhibition of presynaptic D_2 autoreceptors, while the activation of NTS1R within the postsynaptic D_2R decreases the DA signaling (Plach et al., 2019; Cáceda et al., 2006). Several studies suggested the activation of both NTS1 and NTS2 receptors (D_2R inhibition) may stimulate the DA release and DA signaling within the dopaminergic pathway, especially in the SN where both receptors are highly expressed (Mustain et al., 2011; Cáceda et al., 2006). For example, some linear NT analogs showed advantageous effects in reducing motor disturbances and rigidity in an experimental model of Parkinson's disease (PD) in rats, induced with 6-hydroxydopamine (6-OHDA) (Lazarova et al., 2018; Boules et al., 2001). These findings suggest that simultaneous activation of both NTS1R and NTS2R may represent an attractive approach for the treatment of PD, and possibly other neurodegenerative disorders.

Recently, we performed a rational drug design strategy involving a molecular modeling approach to generate favorable modifications of the biologically active fragment of NT, namely NT(8–13) analogs with improved physicochemical properties and enhanced effects *in vivo* (Kühl et al., 2023). In this study, we report *in vitro* pharmacological studies of linear hexapeptides **3** (Lys^8-Cav^9-Pro^{10}-Tyr^{11}-Ile^{12}-Leu^{13}) and **6** (Arg^8-Cav^9-Pro^{10}-Tyr^{11}-Ile^{12}-Leu^{13}) providing their improved stability and permeability compared to the parent peptide NT(8–13) (**2**). Therefore, we further evaluated their ADMET properties *in silico* and investigated the binding interaction situation of peptide mimetics **3** and **6** within both hNTS1R and hNTS2R using a holistic molecular modeling approach, including homology modeling, MD simulations and docking experiments.

2. Results and discussion

2.1. Design and synthesis of peptides 2–7

The linear structure of NT, which comprises 13 amino acid residues (**1**, Fig. 1A), exerts its physiological activity through the C-terminal sequence NT(8–13) (**2**, Fig. 1B) (Carraway and Leeman, 1975; Sefler et al., 1995). Since NT(8–13) (**2**) is a highly potent and selective agonist of NTS1R (K_i hNTS1R = 0.68 ± 0.04 nM and K_i hNTS2R = 1.8 ± 0.17 nM), it is widely considered as a promising lead peptide sequence for the development of NT-based peptide mimetics (Kühl et al., 2023; Keller et al., 2016; Fanelli et al., 2017; Schindler et al., 2019; Keller et al., 2019; Thomas et al., 2014). A major drawback of NT (**1**) and its biologically active fragment NT(8–13) (**2**) is their rapid cleavage *in vivo* by peptidases (half-live below 3 min, cleavage site c1, c2 and c3, *cf.* Fig. 1) (Yeung et al., 2020; Iyer and Kunos, 2021; Kühl et al., 2023; Schindler et al., 2019; Kitabgi et al., 1992). Thus, the majority of the developed synthetic strategies have been focused on NT(8–13)-based mimetics with improved proteolytic stability comprising linear (Keller et al., 2016; Fanelli et al., 2017; Schindler et al., 2019) or macrocyclic structure (Sousbie et al., 2018; Chartier et al., 2021), acting as NTS1R- or NTS2R-selective non-opioid analgesics for potential treatment of acute and chronic pain (Sousbie et al., 2018; Fanelli et al., 2017; Chartier et al., 2021; Dubuc et al., 1999). Considering the advanced research in the field of NTS1R/NTS2R-selective peptide mimetics, we recently reported the development of single or double substituted NT(8–13) analogs using a molecular modeling approach in order to predict and experimentally confirm their activity towards hNTS1R and hNTS2R by radioligand binding assays (Kühl et al., 2023). The aim of our recent study was to develop dual NTS1/NTS2 acting NT(8–13) peptidomimetics, however, with modified N-terminal linear core structure at positions 8 and/or 9 (Fig. 1C) (Kühl et al., 2023).

Peptide NT(8–13) (**2**) and its analogs **3–7** were synthesized by a combined semi-automatic solid-phase peptide synthesis (SPPS) using a 9-fluorenylmethoxycarbonyl (Fmoc) strategy as described previously (Kühl et al., 2023). According to our strategy, peptides **3–7** were obtained via manual coupling of the respective Fmoc-amino acids in positions 8 and 9 followed by Fmoc deprotection and final cleavage from the solid support using the resin-bound tetrapeptide sequence H-PYIL-OH as a starting material (Kühl et al., 2023). The parent hexapeptide NT (8–13) (**2**) was obtained using an automated SPPS continuous flow synthesizer (Kühl et al., 2023). All fully deprotected peptides were purified by semi-preparative RP-HPLC to obtain hexapeptides **2–7** in good to high overall yields, purity, and quantity (Kühl et al., 2023).

Previously *in vivo* studies evidenced that peptide **3** has neuroprotective properties in a mice model of PD and lack of toxicity *in vitro* (Kühl et al., 2023). Furthermore, initial *in silico* studies suggest that the activity towards both NTS1R and NTS2R of NT analogs **3** and **6** is due to the different orientation of their amino acid residues at the N-terminal positions 8 and 9 as compared to the parent peptide NT(8–13) (**2**) (Fig. 2).

Therefore, based on our earlier studies on the N-terminal hexapeptide NT(8–13) (**2**, *cf.* Fig. 1), we intended to further investigate selected peptide mimetics **3** and **6** showing the highest dual bioactivity for their ability to modulate both human NTSRs by performing comparative *in vitro* and molecular modeling studies.

2.2. In vitro stability, protein binding and permeability studies

Improved pharmacokinetic parameters, such as chemical (hydrolytic and time-dependent) and human plasma stability, permeability, and protein binding, are crucial for preclinical investigations and could be a limiting factor for further clinical studies. Therefore, relevant *in vitro* pharmacokinetic studies were performed for selected compounds **3**, **6**, and the reference compound **2**. The obtained results are presented in Table 1 and Fig. 3.

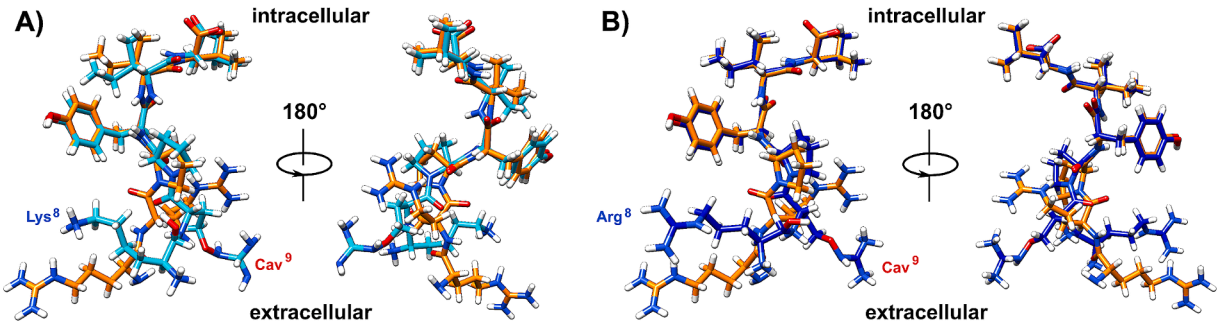

Fig. 2. Superposition and comparison of the binding modes of NT(8–13) (2, in orange) with its peptide analog 3 (A, cyan) and NT(8–13) (2) with peptide 6 (B, blue) as obtained from their conformational states within the active site of the X-ray structure of rat NTS1 receptor bound to NT(8–13) (PDB ID: 4GRV) (White et al., 2012). The 3D receptor structure has been omitted for clarity in order to show the most important amino acid residues at positions 8 and 9 for peptides 3 and 6. Structural visualization was performed with the UCSF Chimera package (http://www.cgl.ucsf.edu/chimera). (For interpretation of the references to color in this figure legend, the reader is referred to the web version of this article.)

Table 1
In vitro stability, protein binding and permeability parameters of **2**, **3** and **6**.

	2	**3**	**6**
Peptide stability (@50 μM)			
% remaining @24 h, pH 2.0 / pH 7.4)	100 / 100	100 / 100	100 / 100
% remaining after 30 days, pH 2.0 / pH 7.4)	> 97 / 100	> 97 / > 100	> 94 / > 95
Plasma stability (@30 min)[a]			
% remaining @10 μM	n.d.	0.48	0.39
% remaining @100 μM (Lit.)	0.02 (< 1.0[b])	0.65	0.22
$t_{1/2}$ (min) @10 / 100 μM (Lit.)	n.d. / < 2.5 (< 2.0[c])	1.8 / 7.3	1.8 / 3.7
PAMPA-BBB permeability [d,e]			
P_e (×10^{-6} cm/s), donor pH 7.4 / acceptor pH 7.4	0.64 ± 0.20	2.81 ± 0.45	0.89 ± 0.10
$-\log P_e$	6.21 ± 0.13	5.55 ± 0.07	6.05 ± 0.03
Plasma Protein Binding (% bound @10 μM) [f]			
	< 1.0	< 1.0	< 1.0

[a]After 5 min incubation time in human plasma at 37 °C. [b] Ref. (Schindler et al., 2019). [c] Ref. (Sarret and Cavelier, 2017). [d] Ref. (Kühl et al., 2023). [e] Data are presented as the main ± SD (n = 3). [f] After 30 min incubation time in human plasma at 37 °C. n.d. = not determined.

At first, we investigated the time-dependent chemical stability of peptides **2**, **3** and **6** after 30 days daylight exposure of samples (50 μM in PBS). Each compound was frequently analyzed by RP-HPLC at 220 nm using an injection volume of 500 μL of each sample. The measurements were performed under physiologically relevant conditions at pH 2.0 and 7.4 (pH-dependent) at room temperature. In accordance to our previous results, peptides **2**, **3**, and **6** were found to be chemically stable at both pH values of 2.0 and 7.4 (Fig. 3A and 3B, Table 1). After 30 days, the percentage of the remaining compound was measured to be 100 % at pH 2.0 and 7.4 for the parent peptide **2** (t_R = 13.5 min), 97 (pH 2.0) and 100 % (pH 7.4) for **3** (t_R = 12.8 min), and 94 (pH 2.0) and 97 % (pH 7.4) for **6** (t_R = 13.4 min) (*cf.* Table 1, Fig. S1). Thus, peptides **2**, **3** and **6** can be used in long-time experiments at physiologically relevant pH ranges, since no remarkable structural changes (hydrolysis and/or photoinduced decomposition) were observed.

Next, we measured the concentration-dependent stability in human plasma (at 10 and 100 μM) of peptides **3** and **6,** and compared them with the results obtained for the reference parent peptide NT(8–13) (**2**) at 100 μM (*cf.* Table 1 and Fig. 3C). The measurements were performed for 180 min under incubation at 37 °C and quantified by LC-MS/MS (*cf.* Fig. S2). The percentage of the respective compound remaining at the individual time points relative to the starting time point (0 min) was calculated from the generated graph (Fig. 3C). The double substituted hexapeptide **3** with the sequence Lys^8-Cav^9-Pro^{10}-Tyr^{11}-Ile^{12}-Leu^{13} (replacement of both Arg residues with Lys^8 and Cav^9) showed concentration-dependent improved stability in human plasma, being two- and three-fold more stable than the parent peptide **2** and its analog **6** (comprising the sequence Arg^8-Cav^9-Pro^{10}-Tyr^{11}-Ile^{12}-Leu^{13} with a Cav residue at position 9 instead of Arg) at a concentration of 100 μM. The results for the reference peptide NT(8–13) (**2**) at the same concentration of 100 μM were comparable with those in the literature (Sarret and Cavelier, 2017; Schindler et al., 2019). Moreover, the plasma protein binding (PPB) analysis of **2**, **3** and **6** revealed a high level of unbound peptide (% unbounded peptide) in human plasma suggesting a high degree of efficacy and potential diffusion across cell membranes (Table 1).

Thus, we further performed BBB permeability studies with peptides **2**, **3**, and **6** by using a parallel artificial membrane permeability assay (PAMPA). PAMPA-BBB is generally used for *in vitro* assessment of a drug's ability to cross the BBB by passive diffusion and, thus, to predict its transcellular and BBB permeability *in vivo* (Kühl et al., 2023; Tzvetkov et al., 2017; Tzvetkov and Antonov, 2017; Chen et al., 2008; Di et al., 2003). PAMPA-BBB experiments with peptides **2**; **3**, and **6** were performed in PBS (at a concentration of 100 μM, pH 7.4 and room temperature) as previously described (*cf.* Table 1, Fig. 3D). According to the obtained results, the double Lys^8/Cav^9-modified analog **3** showed improved ability to cross BBB by passive diffusion with an effective permeability value (P_e) of 2.81 × 10^{-6} cm/s, which was considerably higher than those of the standard drug theophylline (low permeable) and the parent peptide NT(8–13) (**2**, P_e = 0.64 × 10^{-6} cm/s). Thus, the permeability of double-modified analog **3** is higher than the required limit for permeable compounds ($P_e \geq 1.0 \times 10^{-6}$ cm/s) and this peptide could be classified as moderately permeable (Kühl et al., 2023; Di et al., 2003). The Cav^9-modified analog **6** showed higher ability to cross the BBB compared to the parent peptide **2** and the reference drug theophylline, but it is still low BBB permeable when compared with the analog **3** (Table 1, Fig. 3D). The results from the PAMPA-BBB studies were added herein in order to support our previous findings in regard to the overall improved BBB permeability of both NT(8–13) analogs **3** and **6**, and the importance of the double Lys^8/Cav^9-modification in **3** over the single Cav^9 modification in **6** (Kühl et al., 2023).

Summarizing our results from the stability and permeability studies, peptides **3** and **6** were classified as chemically stable with improved human plasma stability and low percentage bound fractions in human protein plasma. On the other hand, peptide **3** showed a better balanced solubility-lipophilicity profile compared to the parent peptide NT(8–13) (**2**) and the single-modified analog **6**, with more than 4-fold increased ability to cross the BB barrier by transcellular passive diffusion as measured for **2** in the PAMPA-BBB experiments. However, peptides could enter the brain by mechanisms other than blood brain penetration such as active influx transport, for example, in addition to passive diffusion (Kühl et al., 2023; Di et al., 2003).

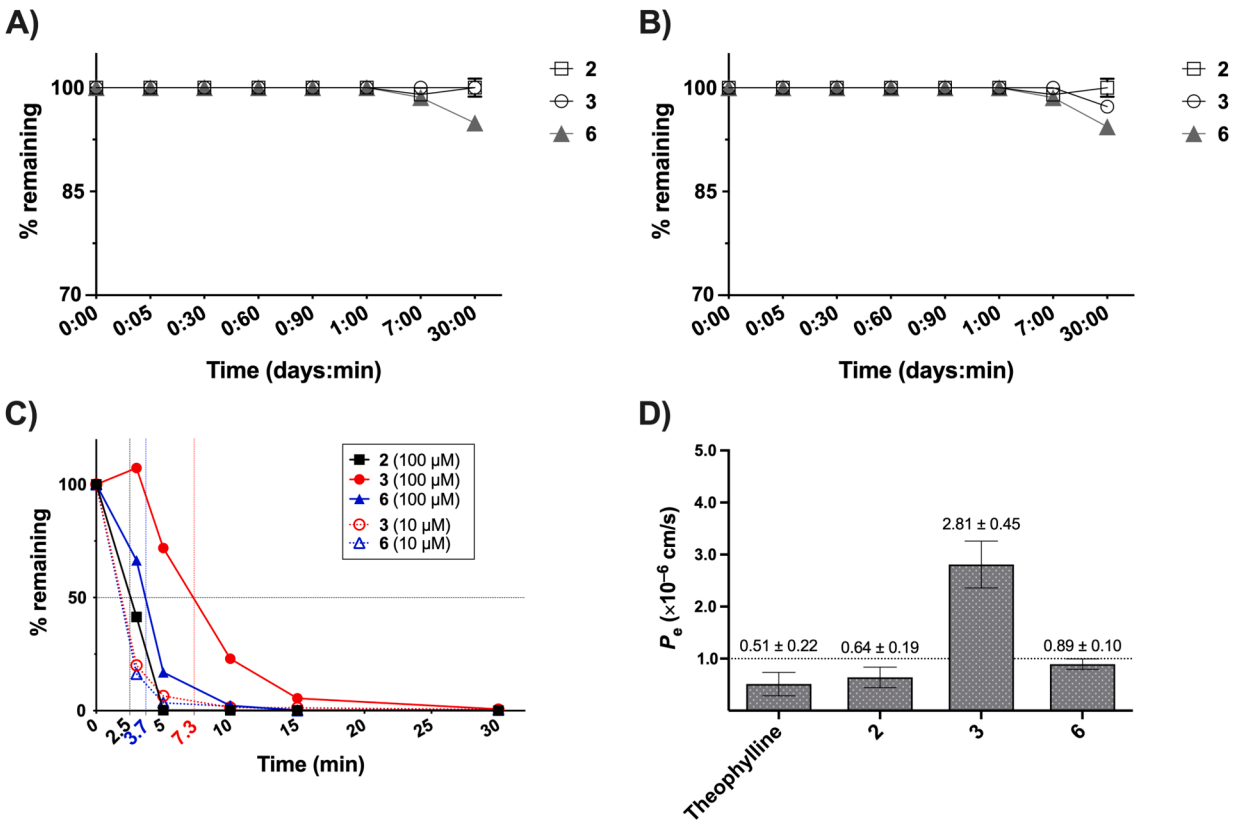

Fig. 3. Time-dependent chemical stability of peptides **2**, **3** and **6** at pH 2.0 (A) and pH 7.4 (B) measured in PBS (50 µM). (C) Stability of **2**, **3** and **6** at a concentration of 10 µM (for **3** and **6**) and 100 µM in human plasma. The plasma half-time at 100 µM of peptides **2**, **3** and **6** is indicated. (D) Distribution of mean BBB permeability of standard drug theophylline, **2**, **3** and **6** measured in the PAMPA-BBB assay. Each data represents the main ± SD ($n = 3$).

2.3. In silico evaluation of physicochemical, drug-likeness, and ADMET properties

In addition to *in vitro* stability, protein binding and permeability experiments, peptide analogs **3** and **6** were further evaluated for their *in silico* physicochemical, drug-like, and ADMET properties in comparison with those of the parent peptide NT(8–13) (**2**) using ADMETlab 0.3 online tool (https://admetlab3-scbdd.com). As expected, both peptide analogs **3** and **6** showed very similar physicochemical characteristics to those of peptide **2** with no significant violations of molecular weight (MW), number of hydrogen acceptors (nHA) and donors (nHD), number of rotatable bonds (nRot) and rings (nRing), number of atoms in the biggest ring (MaxRing), flexibility, number of stereo centers, topological polar surface area (*t*PSA), and predicted solubility (clogS) (Table S1). The majority of these properties are in the optimal range, however, considering the chemical nature of the investigated herein compounds, it is obvious that some of these parameters including MW, number of stereo centers, *t*PSA, and the Van der Waals (VdW) volume, are typical for small peptides rather than for small druggable molecules. It is also not surprising that all three investigated compounds have been predicted to be highly soluble in water with clogS values of –2.327 (for the parent peptide **2**), –1.768 (for **3**), and –2.248 (for **6**), respectively, which is in agreement with their experimentally measured values for aqueous solubility (in mg/mL) at pH 7.4 (Kühl et al., 2023). Based on their structural differences, including amino acid replacement at positions 8 and 9 of analogs **3** and **6** compared to the parent peptide **2** and a different residue at position 9 for peptide mimetics **3** *vs.* **6**, compound **3** possesses the lowest MW, and therefore, lower VdW volume and *t*PSA than the other two peptides.

Although peptides are degraded *in vivo* by peptidases in different tissues, mainly in liver, kidney, gastrointestinal tract, and blood, the parent peptide **2** and its analogs **3** and **6** have also been investigated for their ability to be inhibitors or substrates of Cytochrome P450. The *in silico* evaluation demonstrated that, with exception for compound **3** (a substrate of CYP2C19 and CYP2D6), peptide analog **6** (a substrate of CYP2C19) and the parent peptide **2** (a substrate of CYP3A4), neither of these peptides act as a substrate or an inhibitor of CYP isoenzymes. In addition, all compounds were predicted to possess a high metabolic stability against human liver microsomes (HLM). Furthermore, the drug-likeness and ADMET properties, with a few exceptions for the parent peptide **2**, for all three compounds were predicted to fall within the optimal ranges (overall green and/or rarely orange flags) with no significant violations, in particular, in terms of pharmacokinetic (ADME), general and environmental toxicity, and Tox21 pathway related to a potential activation of cytotoxicity (*cf.* Table S1). Therefore, we selected the double and single modified analogs **3** and **6**, respectively, for further *in silico* studies in order to find an applicable AI-based approach for further design of NT-analogs with improved *in vitro* and *in vivo* stability.

2.4. Molecular modeling studies

Considering their high dual hNTS1R/hNTS2R affinity in combination with improved stability and BBB permeability *in vitro*, peptide analogs **3** and **6** represent promising candidates for further *in vivo* pharmacological evaluation. It is also well-known that, for example, linear peptide analogs of NT(8–13) displayed neuromodulatory and neuroprotective effects by increasing the DA levels as evidenced in rat models of PD (Yeung et al., 2020; Mustain et al., 2011; Cáceda et al., 2006; Lazarova et al., 2018; Boules et al., 2001; Kühl et al., 2023). Therefore, in this work, we applied a successive *in silico* approach, including homology modeling followed by MD simulations and molecular docking experiments, with the aim to generate a stable conformational apo-state of both hNTS1 and hNTS2 receptors, suitable for unconstrained docking experiments for advanced structural exploration

of new designed NT analogs.

The homology models for both receptors were generated based on the existing structure of rat NTS1 receptor in an active-like state (source PDB ID: 4GRV), bound to the full agonist NT(8–13) (**2**). Structural validation of the modeled 3D constructs of hNTS1R and hNTS2R was performed in accordance to an established procedure (Kühl et al., 2023; White et al., 2012). Homology modeling of hNTS1R and hNTS2R was performed after extraction of the full agonist from the entry structure of rNTS1R, *i.e.*, in the ligand-free state of the respective protein. Therefore, the obtained structures of both receptors were used as 3D input files for further MD simulations throughout this study, especially when considering the absence of structural analyses of the human NTS2 receptor.

2.4.1. *MD simulations and post-run analysis*

MD simulations and subsequent post-run analysis were carried out in order to analyse the stability and accuracy of the ligand-free state of hNTS1R and hNTS2R over a period of 400 ns of MD runs (post-run analysis with hNTS2R was also done for the time interval of 800 ns of MD simulations). Analysis of MD trajectories for the respective apo-protein was conducted using topological parameters such as root-mean-square deviation (RMSD) and radius of gyration (Rg). A cluster analysis was also performed to investigate the conformational distribution throughout the respective MD trajectories.

Analysis of RMSD was applied to trace the major backbone deviations under the force field conditions (e.g., TIP3P water model) during the MD simulations. The MD analysis suggest that the ligand-free hNST1 receptor reaches quite rapidly its initial equilibrium after 7.0–8.0 ns (RMSD of 2.190–2.306 nm) with no extremely backbone deviations between 9.0 (2.350 nm) and 27 ns (2.395 nm) (Fig. 4A). After this time of simulation, at the time interval of 29 ns (2.556 nm) occurs the first consistent conformational change which remains constant conserving the structural dynamic over a period of 64 ns (RMSD at 103 ns is 2.694 nm); the receptor is stable and flexible in its conformational state without significant structural fluctuations (see Fig. 4A, inset). In general, hNTS1R showed RMSD values of approximately ~ 2.31–4.52 nm (between 8.0 and 354 ns), while within the time interval of 120 ns (3.084 nm) and 400 ns (4.081 nm), the receptor remains relatively flexible with an average RMSD of about 1.0 nm. The relevant fluctuations of hNTS1R can be attributed to conformational changes and domain movements leading to a spatial unfolding of extra- and intracellular loops with alternating expansions and contractions. Compared to the entire MD interval of 400 ns as for hNTS1R, the MD analysis of the ligand-free hNTS2 receptor reveals a continuous increase of RMSD throughout the time intervals of 20–100 ns (2.479–3.955 nm), 313–338 ns (5.155–5.503 nm), and 342–400 ns (5.363–6.214 nm) with repeating conformational equilibrium (Fig. 4B). The ligand-free hNTS2 receptor reaches its initial equilibrium after 8.0–10 ns (RMSD of 1.946–2.087 nm) of MD simulation, after which the protein structure showed RMSD values ranging from ~ 1.946 to 2.479 nm in the time interval of 8.0–20 ns. After a short period of protein stabilization between 21 and 30 ns (RMSD of 2.530–2.607 nm), the hNST2R showed a slight increase of structural fluctuation with an average RMSD of approximately ~ 1.0 nm in the time interval of 31–96 ns (~2.70–3.70 nm) (Fig. 4B, inset). During the first 126 ns of MD simulation, the ligand-free hNTS2R showed

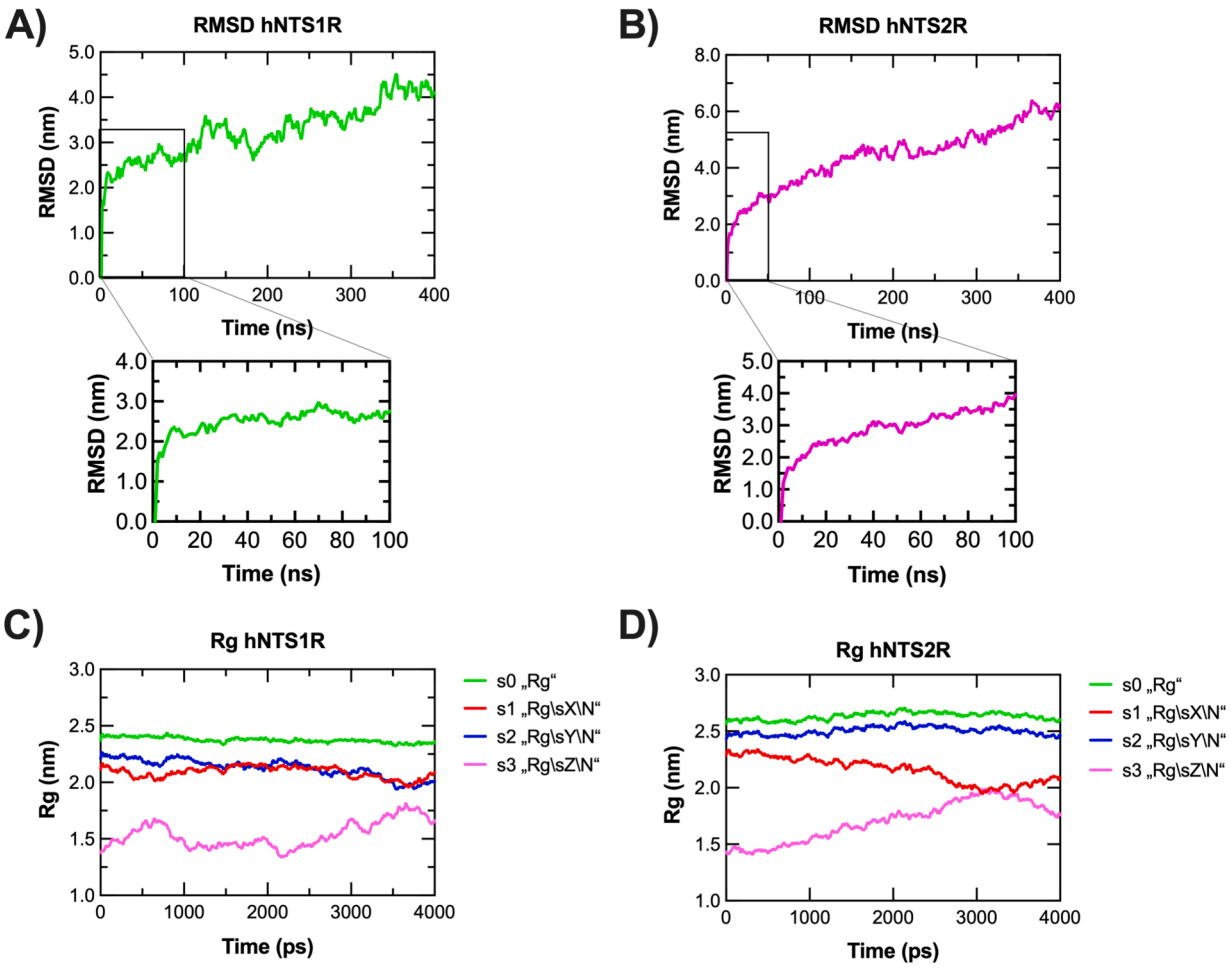

Fig. 4. Representation of RMSD (insets 100 ns) and Rg in 3D environment throughout the respective time interval of MD trajectories obtained after MD simulations with ligand-free state of hNTS1R (400 ns of MD run, panels A and C) and hNTS2R (400 ns of MD run, panels B and D).

tangible conformational changes and movements in the extracellular loops, while the intracellular domain remains rather conserved without extensive fluctuations with RMS deviations between 4.084 nm (126 ns) and 5.095 nm (312 ns). In the time interval of 327–400 ns the protein exhibited average fluctuations of RMS deviations of approximately ~ 0.7 nm, ranging from RMSD of ~ 5.51 to ~ 6.21 nm. A similar situation can be observed for the larger MD trajectory of about 490–800 ns, in which the protein undergoes alternating periods of significant fluctuations followed by conformational stabilization with an average RMSD of approximately ~ 1.0 nm (not shown in Fig. 4B). The MD simulations with hNTS2R suggest that, in contrast to hNTS1R, the significant structural changes associated with conformational rearrangements and domain movements lead to alternated expansions and contractions of the hNTS2R extracellular part, while the intracellular loops undergo contractions. In summary, the RMSD analysis supports the presumed high flexibility of hNTS1 and hNTS2 receptors in their

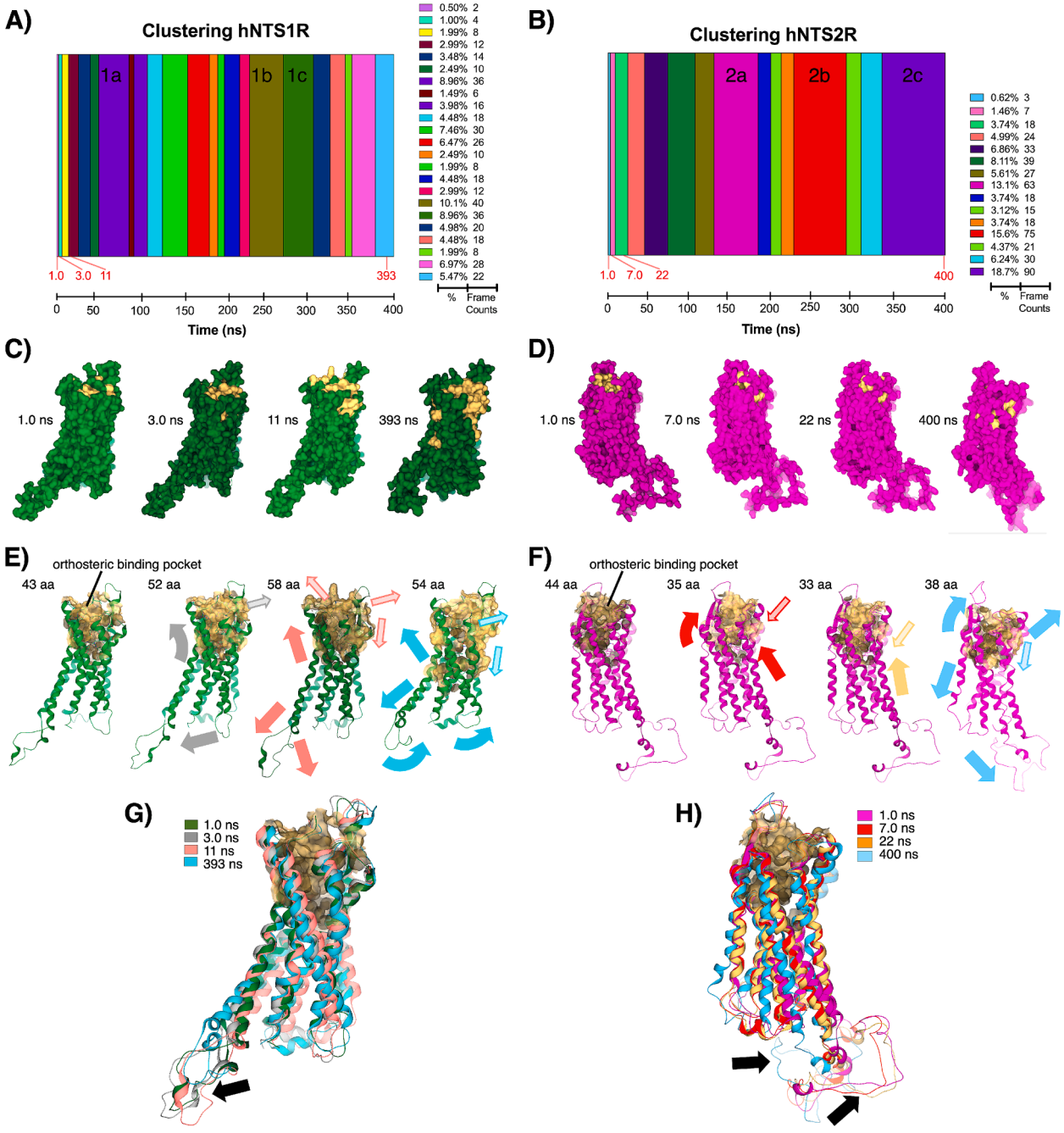

Fig. 5. (A and B) Representation of cluster distribution (incl. cluster percentages and counts, right in panels A and B, as well as the most distributed clusters a-c for each receptor) generated after MD runs at 400 ns with the apo-state of hNTS1R (A) and of hNTS2R (B). The selected time-frames throughout the respective time interval of MD trajectories are indicated in red. (C and D) Corresponding cavity (in deep gold) and protein surface at the appointed time-frames of MD simulations with the apo-state of hNTS1R (C) and hNTS2R (D). (E and F) Visualization of conformational changes of the extracellular orthosteric binding pockets and within the intracellular side of hNTS1R (E) and hNTS2R (F) throughout the depicted time-frames of MD simulations. The significant shifts of the extra-/intracellular site and the orthosteric binding pockets are indicated by correspondingly coloured straight and faded arrows, respectively. (G and H) Overlay of the selected MD time-frame structures of hNTS1R (G) and hNTS2R (H). The significant shifts of the intracellular site towards more expanded (for hNTS1R, G) or more contracted (for hNTS2R, H) conformational state are shown by black straight arrows. (For interpretation of the references to color in this figure legend, the reader is referred to the web version of this article.)

ligand-free state mimicking variable inactive-like conformations.

The RMSD post-run analysis is in good agreement with the radius of gyration (Rg) assessment, quantifying the overall compactness and structural integrity of the proteins in regards to the observed total (green trajectory s0) and around axes X (red s1 trajectory), Y (blue s2 trajectory), and Z (pink s3 trajectory) Rg, as indicated in Fig. 4C and 4D for hNTS1R and hNTS2R, respectively. The Rg analysis revealed that both receptors remain almost compact throughout the whole MD trajectories without considerable structural violations of integrity, as indicated by the green curves for hNTS1R (Fig. 4C) and hNTS2R (Fig. 4D). The average values for the ligand-free states of both proteins were found to be 2.366 ± 0.005 ps (for hNTS1R) and 2.063 ± 0.226 ps (for hNTS2R), indicating preferences of the hNTS1R over the hNTS2R in terms of flexibility (including extra- and intracellular regions/domains) and integrity of the protein over the whole MD trajectory. Furthermore, the course of the red and blue trajectories for hNTS1R indicates of a preferable flexibility of the extra- and intracellular regions compared to hNTS2R, for which the red trajectory decreases from about 2.29 to 2.09 nm throughout the MD simulation of 400 ns. The pink trajectories of hNTS1R and hNTS2R showed different pattern. While for hNTS1R an average Rg value of about 0.20 ps over the MD trajectory can be observed, hNTS2R showed quite different profile with one major violation within the time interval of about 2500–3800 ps and an average Rg value of about 0.33 ps (*cf.* Fig. 4C and 4D). The average Rg value for hNTS1R was found to be 1.6-fold lower than those of hNTS2R throughout the same MD trajectory of 4000 ps (an average Rg of 0.20 *vs.* 0.33 ps). However, the consistent Rg values for hNTS1R suggest that the alpha-helices are compactly arranged within the transmembrane domains, making the hNTS1R more accessible for ligand binding. In contrast, the hNTS2R remain more conservative for ligand binding when comparing the same time interval of 4000 ps as for hNTS1R (*cf.* Fig. 4C and 4D).

RMSD and Rg analysis provided that the ligand-free states of hNTS1R and hNTS2R in general exhibit strongly specific backbone stability profiles, depending on the environmental conditions of the MD simulations performed by using the most commonly used three-point rigid TIP3P water model. In particular, it seems that the surface of hNTS1R is likely lesser destabilized under these aqueous conditions remaining stable and flexible throughout the time interval of MD simulations. In contrast, the hydrophobic surface of hNTS2R showed significantly improved RMSD fluctuations following by a repeated conformational stabilization with subsequent protein folding especially in the intracellular domain through interactions with water molecules. Thus, the RMSD and Rg analysis of the MD trajectories of the ligand-free hNTS1R and hNTS2R is in agreement with the cluster analysis, grouping structurally similar receptor conformations within a cluster over the whole MD simulation (Fig. 5A and 5B). As indicated by the frequent color changes of the clusters in Fig. 5A, hNST1R shows higher flexibility and conformational changes during the 400 ns MD simulation compared to those of hNST2R (Fig. 5B). In general, during the first 50 ns both receptors undergo conformational switches from one to another cluster characterizing distinct conformations within the extra- and intracellular domains, as well, which is no surprising for an apo-state of GPCRs. During this initial time interval of MD simulations, there are 6 and 4 clusters found for hNTS1R and hNST2R, respectively. This situation can be explained with rapid structural rearrangements typically characterized by extracellular loop movements and minor backbone adjustments. Within the 400 ns MD trajectory some clusters appear for very short time intervals, more characteristic for hNST1R rather than hNTS2R, suggesting transient receptor conformations. After the time interval of 50 ns, there were found three more extended clusters for each ligand-free receptor. However, the respective clusters 2a-2c for hNTS2R are more dominantly distributed (each of them with > 10 % contribution to the overall clustering) at the time intervals of ~ 120–180, ~230–300, and ~ 380–400 ns than the respective number of clusters 1c-1c for hNTS1R (only cluster 1b > 10 % contribution) at the time intervals of ~ 60–80 and ~ 230–310 ns, respectively, in which the receptors are stabilized for an extended period (*cf.* Fig. 5A and 5B). Interestingly, both receptors demonstrate similar behavior within the time intervals of ~ 230–310 ns (two clusters for hNST1R *vs.* one for hNTS2R). During the above extended periods, the NTSRs undergo a dynamic stabilization in a single conformation following by repeated rearrangements into the next conformational states. The ligand-free hNTS1R undergoes a higher number of different conformational states, which indicates its more flexible nature when compare to the conservative behavior of hNTS2R within the same interval of 400 ns MD simulations.

Furthermore, we investigated the structural changes within the extra- and intracellular regions of hNTS1R and hNTS2R throughout selected time-frames obtained from the MD simulation with special focus on the orthosteric binding pocket of both proteins. Considering the results from the cluster analysis and after careful inspection of the conformational protein stability, we therefore selected for further computation four distinct time intervals (for each receptor within the MD trajectory of 400 ns) displaying the most flexible conformational changes within the extracellular part of hNTS1R (time-frames at 1.0, 3.0, 11, and 393 ns) and hNTS2R (1.0, 7.0, 22, and 400 ns), respectively. The aim of this experiment was to explore the most plausible receptor conformations, suitable for their activation via agonist binding into the active site of hNTS1R and hNTS2R. It can be seen that the orthosteric binding pocket of hNTS1R undergoes significant structural changes directed outward from the receptor surface, leading to an "open" conformation of its extracellular part in which the number of amino acid residues surrounding the active site of the receptor increases from 43 aa (at 1.0 ns) up to 58 aa (at 11 ns) and remains almost constant throughout the residual MD trajectory (54 aa at 393 ns) (Fig. 5C and 5E). At the same time, a significant extension of the intracellular receptor part can be observed during the whole MD trajectory (Fig. 5G). In contrast, the orthosteric binding pocket of hNTS2R shows a more conserved behaviour throughout the whole MD trajectory. It undergoes a significant movement directed inward the receptor surface, leading rather to a more "closed" conformation of the receptor extracellular part supported by a remarkable decrease of the amino acid residues forming the active site of hNTS2R from 44 aa (at 1.0 ns) to 33 aa (at 22 ns) and their number did not dramatically change (38 aa at 400 ns) throughout the residual MD trajectory (Fig. 5D and 5F). In addition to the extracellular movements, the intracellular site of hNTS2R shifted to highly contracted conformations caused by an altered protein folding (*cf.* Fig. 5H).

2.4.2. *Molecular docking experiments*

To estimate binding affinity of peptides **3** and **6** towards hNTS1R and hNTS2R and to quantify the most stable protein–ligand complexes within the respective MD trajectories, a successive molecular docking approach, including time-dependent docking with subsequent HYdrogen DEsolvation (HYDE) scoring analysis, was applied by using the SeeSAR tool in accordance with previous protocols (Kühl et al., 2023; Tzvetkov et al., 2017; SeeSAR package, Version 13.1 from BioSolveIT GmbH, St. Augustin, 2024). The time-dependent protein–ligand interactions were investigated exploring the intrinsic protein conformations at the above-mentioned time intervals of 1.0, 3.0, 11, and 393 ns for hNTS1R, as well as 1.0, 7.0, 22, and 400 ns for hNTS2R, respectively. The selected time-frames represent the most flexible conformational states of the respective ligand-free protein within the initial 50 and the last 10 ns from the whole 400 ns of MD simulations. As implemented in SeeSAR, the HYDE scoring function calculates realistic free energy of binding (Gibbs free energy, ΔG in kcal/mol) considering the contribution of all non-hydrogen (heavy) atoms to the overall ΔG for both ligand and protein within the respective binding pocket. In addition, HYDE allows to rapidly predict and semi-quantify the binding affinity of peptide mimetics **3** and **6** within the active site of each selected conformation of hNTS1R and hNTS2R. As a result, HYDE calculates the estimated binding affinities and delivers ranges of $K_{i\ HYDE}$ values (HYDE scores/ $K_{i\ HYDE}$ ranging from lower to upper boundaries) and an

approximate lipophilic ligand efficiency (LLE_{HYDE}) for the best-scored docking poses of peptides **3** and **6** within each time-frame of the respective protein–ligand complex (Reulecke et al., 2008; Schneider et al., 2012; Schärfer et al., 2013; Schärfer et al., 2013). Prioritization of the docking results was performed based on integrated in SeeSAR quantifying measures like high binding affinity ranges, torsion, and intra-/intermolecular clash alerts (*cf.* Experimental sections). Based on our results, peptides **3** and **6** showed very high binding affinity ($K_{i\ HYDE}$ values from low pM to low nM) towards both hNTSRs forming strong protein–ligand complexes, obtained with the respective protein conformations at the time interval of 1.0 ns MD run, as confirmed also by green alerts for LLE, intra-/intermolecular clashes, and orange alert for torsions (Fig. 6A and 6B).

As shown in Fig. 6C and 6D, a gradual decrease in binding affinity was observed for peptides **3** and **6** within the protein–ligand complexes modeled with the representative conformations at 3.0 and 11 ns for hNTS1R (with exception of **6** at 11 ns) and 7.0, 22 and 400 ns for hNTS2R, as confirmed by the calculated $\Delta pK_{i\ HYDE}$ values for the respective ligand affinities. Interestingly, both peptides showed a significant increase in binding activity towards the hNTS1R conformation at the time interval of 393 ns of MD simulation ($\Delta pK_{i\ HYDE}$ values of about 5.0), while no binding to hNTS2R at 400 ns was observed. In general, peptide **6** exhibited slightly improved binding activity towards hNTS2R compared with its analog **3**, but following the same trend of affinity profile to both receptors throughout the whole-time interval of MD simulations. In addition, both ligand-free receptors showed notable accessibility to form protein–ligand complexes at their more flexible conformational state at 1.0 ns, which can be considered as an "entry" conformation of hNTS1R and hNTS2R for receptor activation via agonist binding like peptide mimetics **3** and **6** (Kühl et al., 2023).

Therefore, we further compared the obtained conformations of hNTS1R and hNTS2R at the time-frame of 1.0 ns MD run by superimposition of the appropriate 3D structures based on their N-terminal domains (Fig. S3). In fact, both conformations of hNTS1R and hNTS2R in their ligand-free state showed similar orientation of the extracellular part, consisting of three extracellular loops (ECL1-ECL3) and seven transmembrane α-helices (TM1-TM7) (Kühl et al., 2023), but differ in folding and compactness of their intracellular domains. The superposed binding sites of both hNST1R and hNTS2R conformational states revealed their similar 3D architecture within the ECL3/TM7 and ECL3/TM6, but differences in the inner direction of ECL1/TM2 and ECL1/TM3 and thus in the ligand-binding cavity between the 1.0 ns conformational state of hNTS1R and those of hNTS2R. This observation confirms the results from the MD simulations revealing 43 and 44 amino acid residues participating in the formation of the orthosteric binding pocket of hNTS1R and hNTS2R, respectively. Examination of the ligand-receptor binding site of both receptors at the 1.0 ns conformational state revealed the formation of a hydrophobic (S1, ECL1-ECL2) and a hydrophilic subpocket (S2, ECL2-ECL3) within the extracellular end of the receptors together with a second hydrophobic area, however, oriented outward the extracellular loops ECL1-ECL3 (*cf.* Fig. S3).

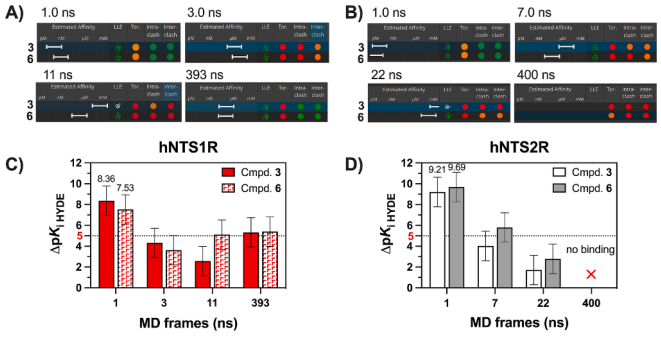

Fig. 6. (A and B) Tabular representation of HYDE time-frame analysis ($K_{i\ HYDE}$ ranges), LLE, torsional, and intra-/intermolecular clashes (as implemented in SeeSAR) for peptides **3** and **6** obtained from their best-scored docking poses within the binding site of hNTS1R (A) and hNTS2R (B) at the respective time-frames of MD simulations. (C and D) Differences in binding affinity ($\Delta pK_{i\ HYDE}$) of peptides **3** and **6** towards the appropriate time-frames obtained from the MD runs with hNTS1R (C) and hNTS2R (D). $\Delta pK_{i\ HYDE}$ values were derived from the respective lower and upper boundaries ($K_{i\ HYDE}$) of HYDE-estimated binding affinities for each receptor–ligand complex. The minimal required pK_i value for drug screening ($pK_i \geq 5.0$) and the highest-estimated median $pK_{i\ HYDE}$ values at 1.0 ns are indicated.

In order to investigate the binding properties of the NT(8–13) analogs **3** and **6** and to analyze the conformational requirement of the ligands that are crucial for activation of both receptors, we subsequently performed docking experiments using the respective conformations of hNTS1R and hNTS2R obtained at the time-frame of 1.0 ns MD simulations. Molecular docking studies were carried out using the same canonical binding site of both receptors (orthosteric binding pocket) as confirmed from the cryo-EM structure of hNTS1R-G_{i1} (PDB ID: 60S9) in complex with the potent NTS1R agonist JMV449 (Kato et al., 2019), which provides a useful information about the 3D architecture and binding properties of the ligand within the extracellular part of hNST1R. Since the extracellular part of hNTS1R and hNTS2R at their "entry" conformational state of 1.0 ns MD simulations is almost similar (*cf.* Fig. S3), with some differences in ECL1/TM2 and TM3, we used the 2D-NMR structures of peptides **3** and **6** as PDB input structures in SeeSAR to predict the putative binding modes and binding affinities of both investigated NT-analogs (SeeSAR package, Version 13.1 from BioSolveIT GmbH, St. Augustin, 2024; Kühl et al., 2023). The docking experiments performed herein provided valuable information regarding the common interactions within the obtained ligand-receptor binding modes of peptides **3** and **6** with respect to their ability to activate both NTSRs, as experimentally confirmed to be hNTS1R agonists (Kühl et al., 2023). In general, the binding modes and estimated affinities evidenced that both NT analogs **3** and **6** occupy the same ligand-binding cavity space within hNTS1R surrounded by amino acid residues located between ECL1 and ECL3 (Fig. 7A). In contrast to peptide **3** (similar binding within both receptors), the NT analog **6** engaged a different ligand-binding cavity within hNTS2R with actively participation of amino acid residues from ECL1 and ECL2 (Fig. 7C).

Moreover, both peptides showed the same orientation and very good overlap of the common C-terminal sequence (Pro^{10}-Tyr^{11}-Ile^{12}-Leu^{13}) into the more lipophilic region inside the binding pockets of the receptors, with the amino residues at positions 8 (Lys for **3** *vs.* Arg for **6**) and 9 (Cav for **3** and **6**) pointing outwards the receptor surface. Based on the obtained binding modes, both peptides showed different conformations and orientations at their N-terminal amino acids at positions 8 and 9 within the binding cavity space close to the extracellular end of both receptors (Fig. 7B and 7D). In addition, the time-dependent docking experiments with selected time-frames of MD simulations suggest that the receptor activation occurs via a ligand-receptor binding into the "entry" conformations of hNTS1R and hNTS2R within the time interval of 1.0–3.0 ns of their ligand-free state.

2.4.3. Molecular docking analysis

To predict the binding affinity and thus to estimate the thermodynamic profile of peptides **3** and **6** within the binding pocket of NTSRs, we performed a comparative analysis of binding interactions and HYDE visual assessment of binding of the best ranked docking poses of both peptides in the "entry" conformations of hNTS1R and hNTS2R at the time-frame of 1.0 ns MD simulation. Considering the binding situation for both peptides in hNTS1R it can be seen that their C-terminal tetrapeptide sequence engages a binding pocket surrounded by hydrophobic amino acid residues. Both ligands formed important hydrophobic interactions (16 for **3** *vs.* 14 for **6**) with Phe^{75}, Val^{171}, Tyr^{287}, His^{291}, and Tyr^{294}, as well as common hydrogen bonds with Leu^{2}, Tyr^{93}, Arg^{270}, Phe^{274}, Tyr^{290}, and Trp^{282} (except **6**), all of them located in TM1, TM3, TM6, and TM7 (Fig. 8A, Table S2).

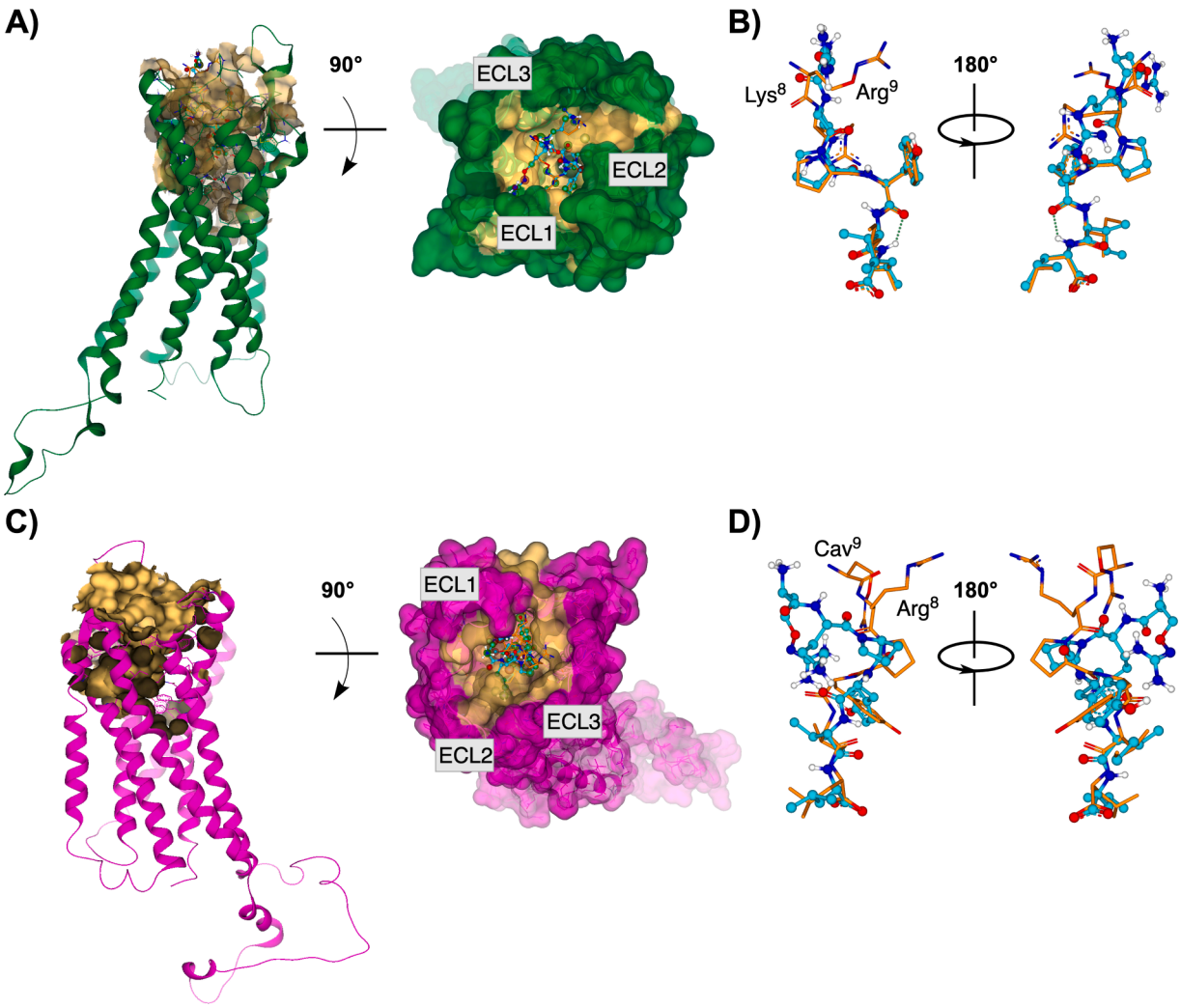

Fig. 7. (A and C) Visualization of ligand-binding pockets (in deep gold) and the docking models of peptides **3** and **6** obtained from their best-scored docking poses into hNTS1R (A, green) and hNTS2R (C, magenta). The docking models were generated with the representative receptor structures preserved at the time interval of 1.0 ns of MD simulations with apo states of the homology modeled hNTS1R or hNTS2R. In (A) and (C), the respective receptor backbone is presented as ribbons (left) and with transparent protein surface (right), obtained by a rotation of ca. 90° around the vertical. The extracellular loops for each receptor ECL1-ECL3 are indicated. (B and D) Comparison of the docking models of peptides **3** (represented in cyan balls and sticks) and **6** (orange sticks) obtained after superimposition of the hNTS1R–ligand (B) and hNTS2R–ligand (D) complexes, respectively. The receptor has been omitted for clarity and the residues at positions 8 and 9 for peptide **6** are highlighted. (For interpretation of the references to color in this figure legend, the reader is referred to the web version of this article.)

The docking models and HYDE visual assessment of binding for **3** and **6** in hNTS1R suggested a higher thermodynamic stabilization with more favorable conformation of their C-terminal tetrapeptide sequence Pro^{10}-Tyr^{11}-Ile^{12}-Leu^{13} via formation of an intramolecular H-bond with a distance of 2.10Å (for **3**) and 2.24Å (for **6**), respectively (Fig. 8A). In this lower part of the extracellular sub-pocket within the TM3, TM6 and TM7 both peptides formed common H-bonds with Tyr^{93}, Phe^{274}, Tyr^{290} and the residue Arg^{270}, which contributed to an additional conformational stabilization of the ligands via formation of H-bonds with Phe^{274} and Tyr^{290}. Interestingly, the residue Phe^{274} forms two H-bonds with peptide **3** and one with **6**, serving at the same time as a hydrophilic H-bond acceptor and hydrophobic pi-donor (*cf.* Table S2). However, the best scored docking poses of **3** and **6** displayed major differences in their N-terminal conformation with the residues at positions 8 and 9 showing a different orientation in the upper part of the extracellular sub-pocket. Compound **3** comprising Lys^{8} and Cav^{9} amino acid residues at its N-terminus seems to be involved in the formation of more H-bonds within the binding site of the hNTS1 receptor, than its analog **6** with Arg^{8} and Cav^{9} (*7 vs.* 5H-bonds). While peptide **3** forms two H bonds with Phe^{274} and one strong H-bond with Trp282, compound **6** interacts via one H-bond with Phe^{274} and establishes strong hydrophobic pi-alkyl interactions with Trp^{282} and Tyr^{287} within the same binding cavity of hNTS1R (Fig. 8A).

The best-scored docking poses for **3** and **6** in hNTS2R suggested that, similarly to their binding modes to hNTS1R, the C-terminal tetrapeptide sequence Pro^{10}-Tyr^{11}-Ile^{12}-Leu^{13} of the ligands occupies a binding sub-pocket surrounded mainly by hydrophobic residues from TM2, TM3 and TM6 (Fig. 8B). Therefore, the binding modes of both ligands revealed the formation of hydrophobic interactions (9 for **3** *vs.* 7 for **6**) with Tyr^{297}, Tyr^{310}, Tyr^{313}, His^{314} and Tyr^{294} for both peptides, as well as with Tyr^{317} and Val^{170} for peptide **3** (Table S2). Common H-bonds for both ligands were observed with residues Tyr^{89}, Tyr^{297}, Tyr^{313} and Arg^{293} within the binding pocket of hNTS2R. The binding mode of peptide **6** with Arg^{8} and Cav^{9} at its N-terminus showed the formation of more H-bonds than compound **3** (8 *vs.* 10*H*-bonds). While compound **3** interacts via two strong H-bonds with Tyr^{297} and forms single H-bonds with His^{75} and His^{314} in the orthosteric cavity of hNTS2R, the peptide analog **6** establish additionally H-bonds with Phe^{71} and Thr^{172} within the lower part of the binding pocket as well as with Gly^{1}, Leu^{157}, and Trp^{305} in the upper part of the extracellular sub-pocket (*cf.* Fig. 8B). In

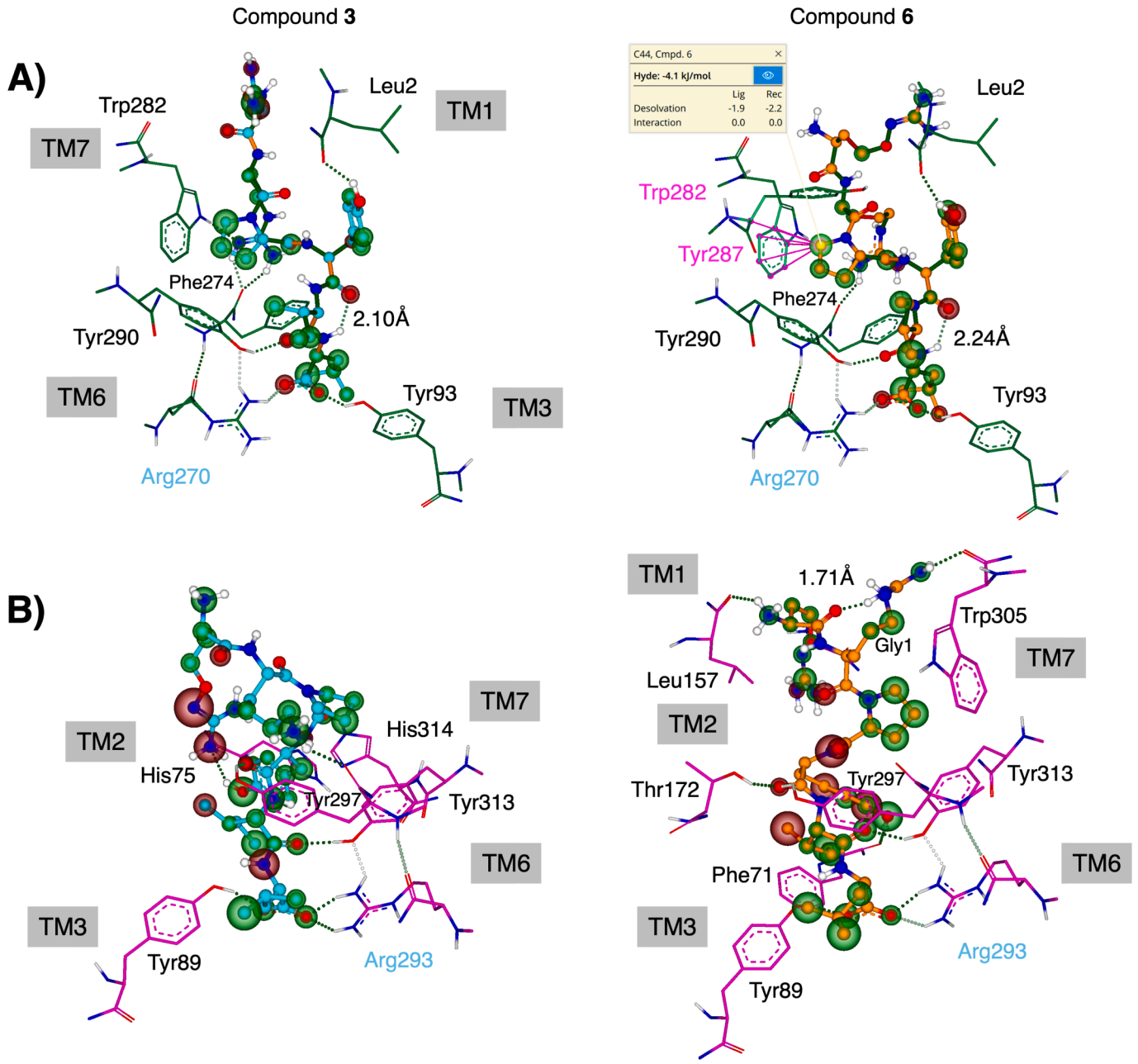

Fig. 8. Docking models and HYDE visual assessment of binding (as implemented in SeeSAR) for the best-ranked poses of NT analogs **3** (left, cyan balls and sticks) and **6** (right, orange balls and sticks) obtained at the time interval of 1.0 ns of MD simulation with hNTS1R (A, green) and hNTS2R (B, magenta). The receptor residues and the transmembrane α-helices (TM1–TM3, TM6 and TM7) involved in H-bonding (dotted lines) are shown as wire-frame indicated in black, those forming pi-sticking interactions in magenta, and the residues Arg270 (for hNTS1R) and Arg293 (for hNTS2R), representing a combination of salt-bridge formation and electrostatic H-bond, are represented in slight blue. HYDE visual affinity assessment: green = favorable, red = unfavorable and non-colored = not relevant for binding affinity. The numbering of receptor residues is based on the homology modeled 3D structures of hNTS1R or hNTS2R used for MD simulations. Note that the orientation of ligand-binding pockets is the same as in Fig. 7. (For interpretation of the references to color in this figure legend, the reader is referred to the web version of this article.)

addition to the greater number of H-bonds, peptide **6** establish one intramolecular bond of 1.71Å between its N-terminal residues Arg^{8} and Cav^{9}, while no intramolecular bonds were found for analog **3**, accounting for the slightly higher binding affinity of **6** to hNTS2R compared to those of compound **3**. Similar to the binding modes of **3** and **6** in hNTS1R, the residue Arg^{293} plays an important role for the conformational stabilization of the ligands via salt bridge formation with Tyr^{297} and Tyr^{313}, contributing to the overall binding affinity of both peptides towards hNTS2R.

As aforementioned, the computed binding modes of the ligands within the binding pockets of hNTS1R and hNTS2R suggested different conformations and orientation of their N-terminal residues Lys^{8}/Cav^{9} (for peptide **3**) and Arg^{8}/Cav^{9} (for **6**), leading to an extension of the extracellular space of the receptor–peptide complex. In general, the estimated binding affinity of both NT-analogs seems to be embossed by the formation of H-bonds mainly with arginine, tyrosine and phenylalanine residues as well as hydrophobic interactions within the lower part of the binding pockets of both receptors.

2.4.4. Comparison between experimental and estimated binding affinities

In order to confirm the estimated binding affinities of peptides **3** and **6** against both NTSRs, we compared the computed in SeeSAR binding affinities for the best "entry" docking poses at time-frames of 1.0 ns of both NT analogs with those obtained from the radioligand binding essays. Radioligand binding experiments were performed as previously described using HEK293 (human embryonic kidney 293) cells for hNTS1R or hNTS2R expression and [Leu^{3}H]NT(8–13) as a radioligand (Kühl et al., 2023). The scoring function HYDE in SeeSAR was used to predict binding affinities (expressed as $K_{i\ HYDE}$ ranges) of peptides **3** and **6** towards hNTS1R and hNTS2R (*cf.* Experimental section). The experimental and the predicted binding affinities as well as the hNTS1R/hNTS2R selectivity (expressed as SI) are collected in Table 2. Overall, the binding models of peptides **3** and **6** to hNTS1R and hNTS2R reproduced their experimentally obtained binding affinities to both receptors (expressed as K_i values). Importantly, the predicted $K_{i\ HYDE}$ ranges (from low nM to pM) for the best-scored docking poses of both compounds within the binding pocket of the potential "entry" conformations of hNTS1R and hNTS2R at the time-frame of 1.0 ns MD simulation are in agreement with the experiment. For comparison, the experimental K_i values for **3** and **6** were found to be in the low nanomolar range (for **3**: K_i hNTS1R = 6.9 ± 0.59 nM and K_i hNTS2R = 6.5 ± 0.63 nM; for **6**: K_i hNTS1R = 5.5 ± 1.7 nM and K_i hNTS2R = 5.6 ± 1.0 nM), however, all of them within the HYDE estimated $K_{i\ HYDE}$ ranges (for **3**: 0.43–43.2 nM at hNTS1R and 6.13–609 nM at hNTS2R; for **6**: 2.95–293 nM at hNTS1R and 1.16–115 nM at hNTS2R). The experimental data confirm that both NT analogs are equally selective at both NTSRs with SI = 1.06 and 0.98 for **3** and **6**, respectively. The double substitution of Arg^8/Arg^9 by Lys^8 and Cav^9 in the core structure of NT(8–13) (peptide **3**) led to a slight decrease in binding affinity compared to the corresponding single replacement of Arg^9 by Cav^9 in peptide **6** while keeping the high potency (low nM range) and selectivity towards both NTSRs (*cf.* Table 2). Considering the common substitution of Arg^9 by Cav^9 in both NT(8–13) analogs it can be concluded that a canavanine (Cav) residue at position 9 mimicking the guanidine function and the alkyl chain of arginine as well as a lipophilic amino acid at position 8 such as lysine at the N-terminus of peptide **3** are well-tolerated regarding binding affinity and receptor selectivity toward both NTSRs.

In summary, the molecular modeling studies herein are in agreement with our previous observations (Kühl et al., 2023) suggesting that substitutions at Arg^8 by Lys (in peptide **3**) and at Arg^9 by Cav (for both peptides **3** and **6**) of the biologically active NT fragment 8–13 (**2**) lead to dually active analogs against hNTS1R and hNTS2R with experimentally confirmed binding affinities in the low nanomolar range. Furthermore, it can be assumed that both NT analogs are able to mimic the main interactions of the parent peptide NT(8–13) within the binding site of both human NTSRs with similar biological properties as the native peptide NT (Kühl et al., 2023). Moreover, the different orientation of Lys^8/Arg^8 and Cav^9 within the upper extracellular part of the NTSRs could explain the slight differences in binding affinity of both hexapeptide analogs **3** and **6** toward hNTS1R and hNTS2R. In addition, the comprehensive *in silico* investigations applied in this work suggest that the receptor activation most likely occurs via a ligand-receptor binding into the potential "entry" conformation of hNTS1R and hNTS2R, as confirmed by analysis of the respective MD trajectories and binding affinity experiments.

Table 2
Experimental and predicted binding data for hNTS1R and hNTS2R of ligands **3** and **6**.

	Receptor	3 H-Lys^8-Cav^9-Pro-Tyr-Ile-Leu-OH	6 H-Arg^8-Cav^9-Pro-Tyr-Ile-Leu-OH
EXPERIMENT			
K_i binding (nM) [a]	hNTS1R	6.9 ± 0.59	5.5 ± 1.7
	hNTS2R	6.5 ± 0.63	5.6 ± 1.0
SI	*Ki* (hNTS1R) / *Ki* (hNTS2R)	1.06	0.98
PREDICTION [b,c]			
$K_{i\ HYDE}$ range (nM)	hNTS1R	0.43–43.2	2.95–293
	hNTS2R	6.13–609	1.16–115

[a] Determined by radioligand competition binding with [^{3}H]**2** at HEK293T cells; unless otherwise stated, the K_i values in nM ± SEM are the means of three (at hNTS1R) or four (for hNTS2R) individual experiments, each performed in triplicate (Ref. (Kühl et al., 2023). [b] Estimated HYDE K_i range values using SeeSAR (SeeSAR package, Version 13.1 from BioSolveIT GmbH, St. Augustin, 2024). [c] $K_{i\ HYDE}$ ranges only for the selected/best docking poses from the molecular docking experiments performed with the protein frames at 1.0 ns obtained from the MD simulations for both human NTSRs. SI = selectivity index.

3. Conclusion

In the present study, we investigated two linear peptide analogs of the biologically active NT(8–13) peptide (**2**) aiming at *in vitro* and *in silico* evaluation of their pharmacological potential as dual-acting hNTS1R and hNTS2R ligands for the treatment of Parkinson's disease (PD) and probably other related disorders. The peptide analogs possessed modifications at the N-terminal positions 8 and/or 9 obtained via replacement of Arg^9 with Cav (for peptides **3** and **6**) and/or Arg^8 with Lys (for peptide **3**) residues in the parent peptide **2**, leading to an equipotent affinity at both hNTS1 and hNTS2 receptors. Based on their experimental binding affinities (K_i values in low nM range) combined with improved pharmacological profile, including human plasma and chemical stability, as well as BBB permeability, peptide analogs **3** (comprising the sequence Lys^8-Cav^9-Pro^{10}-Tyr^{11}-Ile^{12}-Leu^{13}) and **6** (Arg^8-Cav^9-Pro^{10}-Tyr^{11}-Ile^{12}-Leu^{13}) were selected for extended *in silico* ADMET evaluation and molecular modeling studies. Therefore, we applied an AI-based approach to generate the homology models of hNTS1R and hNTS2R, followed by MD simulations of their ligand-free state and Molecular Docking in order to estimate the most probable protein–ligand complexes of peptides **3** and **6**. The binding interaction/affinity analysis of the best-ranked docking poses, obtained with selected time-frames from the respective MD trajectories, suggest that the receptors activation occurs via a ligand-receptor binding into the potential "entry" conformation of hNTS1R and hNTS2R at the time-frame of 1.0 ns MD simulation. Further HYDE analysis of binding confirmed the binding affinities of **3** and **6** towards hNTS1R and hNTS2R and are in agreement with those obtained by radioligand binding experiments. This study represents a comprehensive *in silico* approach that offers additional options to the use of 3D structures, and may potentially serve for further development of dually active NT peptide mimetics, especially in the case of hNTS2R. However, it should be considered that the long-term stability of linear peptide mimetics under physiological conditions is crucial for *in vivo* applications of such NT analogs suggesting a focus for future research on peptide-based compounds with improved physicochemical parameters to be of a great promise. Therefore, it will be of great interest to investigate the effects of structurally related NT analogs in suitable *in vivo* models, as for example, for their analgesic properties, as well as neuropharmacological efficacy against Alzheimer's disease or Schizophrenia in addition to their efficacy against Parkinson's disease.

4. Experimental section

4.1. Synthesis, purification and characterization of peptides 2–7

Synthesis of NT(8–13) (**2**) and peptides **3–7** was performed by automated solid-phase peptide synthesis (SPPS) on a ResPep SL peptide synthesizer (Intavis Bioanalytical Instruments AG, Cologne, Germany) in accordance to a semi-automatic Fmoc (*N*-(9-fluorenyl)methoxycarbonyl) protocol. The crude peptides were purified and further characterized as described earlier (Kühl et al., 2023; Kühl et al., 2013; Brewitz et al., 2015; Heimer et al., 2018).

4.2. Chemical stability studies

Control of chemical stability of peptides **2**, **3**, and **6** was performed by RP-HPLC analysis (for time-dependent stability, after 30 days) of the stock solutions stored at room temperature and under exposure to daylight. The RP-HPLC stability control experiments were performed with a volume of 500 μL of a 50 μM PBS stock solution using a Shimadzu LC-20A HPLC system equipped with a Vydac218TP54 C18-RP column (250 × 4.6 mm, particle size 5.0 μm). The elution was performed with an eluent mixture of water containing 0.1 % TFA (eluent A)/acetonitrile containing 0.1 % TFA (eluent B) by gradient 15 % to 45 % for 30 min at a flow rate of 1.0 mL/min. UV absorption was detected at 220 nm using DAD. The obtained results were compared with the respective original spectra of the pure peptides (*cf.* Fig. S1).

4.3. Plasma stability studies

Plasma stability was measured by fortifying 10 and 100 μM of the test peptides **2**, **3** and **6,** each to freshly thawed commercially available plasma aliquots of 1.0 mL (Pooled Normal Human Plasma, innovative research, Peary Court Novi, MI, United States). After the time points of 0, 3.0, 5.0, 10, 15, 30, 45, 60, 90, 120, 150, and 180 min incubation at 37 °C, 50 μL of the samples were transferred to reaction tubes, diluted 1:100 with 0.2 % formic acid, and quantified by LC-MS/MS. The measurements were conducted using a high-performance liquid chromatograph (Shimadzu Nexera, Duisburg, Germany) coupled to a SCIEX QTRAP 6500 mass spectrometer (Darmstadt, Germany). After incubation time of 5 min, the percentage of each test compound remaining at the individual time points relative to the starting time point (0 min) was then calculated (*cf.* Fig. S2).

4.4. Parallel artificial membrane permeability assay (PAMPA)

Determination of blood–brain barrier (BBB) permeability of peptides (NT(8–13) (**2**), **3** and **6**, and the standard drug theophylline was performed using PAMPA Explorer kit (Pion Inc., Billerica, MA, USA) by measuring the UV–VIS absorbance of compounds in both donor and acceptor compartments (White et al., 2012; Tzvetkov et al., 2017). Stock solutions of investigated peptides (10 mM) were prepared in $PBS_{7.4}$ and for standard drugs in DMSO (10 mM and 50 mM for lidocaine). The corresponding stock solutions were diluted to a final concentration of 100 μM (for peptides **2**, **3** and **6**) and 50 μM (5.0 μL/well, 1.0 % v/v final DMSO concentration for theophylline) with Prisma HT buffer solution (pH 7.4) in ddH_2O. The resulting solution (200 μL) was added to each well of the donor plate ($n \geq 6$) and a "sandwich" plate was prepared. The measurements of PAMPA-BBB permeability were performed as previously described (Kühl et al., 2023; White et al., 2012; Tzvetkov et al., 2017). The absorbance spectra (250–500 nm) of the solutions in the blank, acceptor, and donor plates were obtained using an Epoch microplate reader. The P_e and $-\log P_e$ values were automatically processed with the PAMPA Explorer software v.3.8 (Pion). The data are presented as the mean values ± SD of three independent experiments.

4.5. Plasma protein binding (PPB)

4.5.1. PPB assay

For PPB studies, human plasma (total volume 200 μL) was enriched with the peptides **2**, **3** and **6** (10 μM) and incubated at 37 °C for 5 min for PPB equilibrium. The peptide containing plasma probes were transferred into 500 μL 30 kDa MWCO filter devices (Amicon Ultra, Merck, Darmstadt) and filled up with 300 μL PBS buffer. The devices were centrifuged at 14,000 rcf for 15 min and subsequently washed with 500 μL of PBS buffer. After the elution of the filter concentrate, the slurry was reconstituted with PBS buffer to an exact final volume of 200 μL. The PPB samples as well as the reference (10 or 100 μM of the peptide in 200 μL PBS) were diluted 1:100 with 0.2 % formic acid and finally measured via LC-MS/MS.

4.5.2. Analysis of PPB assay

For analysis of the PPB studies, a Shimadzu Nexera HPLC system (Duisburg, Germany) coupled to a SCIEX QTRAP 6500 mass spectrometer (Darmstadt, Germany) was used. The eluent mixture included eluent A (0.2 % formic acid, pH 2.5) and eluent B (acetonitrile). The analytical system was equipped with a Thermo Fisher Acclaim Polar Advantage II analytical column (3 x 100 mm, 3 μm particle size, Dreieich, Germany) with a flow rate of 400 μL/min, a gradient of 1–100 % of eluent B over 11 min. For every measurement, the mass spectrometer was operated in high mass positive electrospray ionization mode with a needle voltage of 5.0 kV. Nitrogen was used as a collision gas. Optimized Multiple Reaction Monitoring (MRM) experiments were performed on the most abundant ion transitions, which were identified by direct infusion of reference solution and software-based optimization for each peptide.

4.6. Computational methods

4.6.1. In silico evaluation of physicochemical, drug-likeness, and pharmacokinetic properties

The SMILES strings for the investigated peptides were used as input data for evaluation of their physicochemical, drug-like, pharmacokinetic (ADME), and toxicological (T) properties by implementation of the ADMETlab 0.3 online tool (https://admetlab3.scbdd.com, accessed on November 11, 2024). The ADMET evaluation function module of ADMETlab 3.0 tool incorporates several high-quality predictive models constructed by the Directed Message Passing Neutral Network (D-MPNN) framework, enabled to predict 21 physicochemical properties, 19 drug-like, 34 pharmacokinetic endpoints, 36 toxicity endpoints, and 8 toxicophore rules (https://admetlab3.scbdd.com/).

4.6.2. Homology modeling

The 3D structures of human NTS1 and human NTS2 receptors were modeled as previously described (Kühl et al., 2023) using the respective sequences (P30989 / hNTS1R and O95665 / hNTS2R) retrieved from the UniProt database (https://www.uniprot.org/). A target-template alignment was performed with the high-resolution (2.80 Å) crystal structure of the rat NTS1 receptor in complex with NT(8–13) peptide (PDB ID: 4GRV) (White et al., 2012) used as an input structure for homology model building of the hNTS1 receptor. The respective ligand NT(8–13) presented in the template structure was not transferred to the homology model of hNTS1R. The homology models of both receptors were automatically generated via the homology model building protocol using the SWISS-MODEL server (https://swissmodel.expasy.org/). The generated 3D structures of human NTS1 and NTS2 receptors were found to be 84 and 40 % identical with the initial template sequence, respectively. During the homology model building, conserved coordinates between the target and the template sequences were transferred from the template to the model, while insertions and deletions were remodeled. The homology modeled human NTS1 receptor displayed almost full alignment with the extracellular side and significant differences in the intracellular loops of the rNTS1 receptor, which is evidence of a good complementarity between the X-ray structure of rat and the homology model of hNTS1R. In addition, side chains were rebuilt and their geometries optimized, and the overall quality was assessed using the QMEAN scoring function (Studer et al., 2020). Among the 50 models obtained for each receptor, only those with the highest quality (for hNTS1R: rNTS1R *vs.* homology modeled hNTS1R) and better coverage score (for hNTS2R: rNTS2R *vs.* homology modeled hNTS2R) were selected for further computations. Finally, quality check of the homology model for hNTS1R was performed by structural alignment between the PDB structures of human and rat NTS1R using MultiSeq functionality (Roberts et al., 2006) implemented in the VMD software (https://www.ks.uiuc.edu/Research/vmd/). The homology models of hNTS1R and

hNTS2R were used as the target-input PDB structures for further molecular dynamics (MD) simulations in this study without further structural modifications.

4.6.3. Molecular dynamics simulations

Molecular dynamics (MD) simulations were performed with the homology models of hNTS1R and hNTS2R in their ligand-free state using GROMACS version 2023.3 tool (https://www.gromacs.org). The MD simulations were conducted applying the OPLS-AA/L all-atom force field 1 (2001 amino acid dihedrals), as implemented in GROMACS version 2023.3. The topology and parameter files of the input PDB structures of hNTS1R and hNTS2R were generated following the guidelines included in GROMACS version 2023.3 manual. Accordingly, the size (XYZ length in Å) and type of the "box" embedding the protein were defined. A cubic box, in which the respective protein was placed in the middle of this box at a minimal distance of 1.0 nm from each of its edges, was created in order to ensure a minimum of 20Å increase within the "Box XYZ length in Å" and to avoid any interactions between periodic images of the protein during the MD simulation. Consequently, the input file with the protein coordinates and the source file containing the respective hNTS1R or hNTS2R in the box were determined. A TIP3P water model was used to solvate the system and to fill the box, the respective K^+ and Cl^- ions (100 mM) were added in order to neutralize the net charge of the protein. The topology file of the respective protein was automatically updated by GROMACS. After solvation and chemical neutralization of the system, energy minimization (EM) of the respective protein was performed using the Steepest Descents algorithm implemented in GROMACS. After this step, the protein structure was optimized by removing steric clashes and improving its geometry, and the respective hNTS1R and hNTS2R was ready-to-use for MD simulation. The system was subjected to two-step equilibration including canonical NVT (isothermal-isochoric ensemble) and NPT ensemble (isothermal-isobaric ensemble). After completing the equilibration steps and the system has reached the desired temperature and pressure conditions, initial MD runs for 4.0 and 50 ns (for hNTS1R) and for 4.0, 10, 40, and 100 ns (for hNTS2R) were performed to validate the respective MD system, prior to accomplishing the MD simulations for 400 ns (for hNTS1R) and 800 ns (for hNTS2R) with 2.0 fs (femtoseconds) steps. Visualization of MD simulations and analysis of the results were processed with USCF Chimera v1.18 (https://www.cgl.ucsf.edu/chimera/) tool using the respective MD.trp and MD.xtc output files from each MD run within the MD movie panel of Chimera and saved as output *mp4 files (see also Supporting files 1 and 2).

4.6.4. Post-analysis of molecular simulation data

MD simulation post-analysis was carried out in order to analyse the stability and accuracy of the ligand-free hNTS1R and hNTS2R over the whole period of MD simulation of 400 or 800 ns, respectively. Analysis of MD trajectories for the respective ligand-free protein was performed based on selected topological parameters including root-mean-square deviation (RMSD) and radius of gyration (Rg). A cluster analysis was conducted with all generated frames during the MD simulations with both proteins. The complete clustering was constructed for the whole-time interval of 400 or 800 ns of MD trajectory in order to find the most stable conformations for longer period of time of the hNTS1 or hNTS2 receptor, respectively. The related graphs (RMSD, Rg and clustering) were plotted by using GraphPad Prism v6.0 (GraphPad Software, La Jolla, CA, USA). For this reason, the extracted data files rmsd.xvg and gyrate.xvg obtained from the MD simulation with GROMACS were applied for MD trajectory analysis, while the automatically generated with USCF Chimera v1.18 (https://www.cgl.ucsf.edu/chimera/) cluster.txt files were used for semi-manual performing of cluster analysis throughout the whole time interval of 400 ns (for hNTS1R) or 800 ns (for hNTS2R) of MD trajectory.

4.6.5. Molecular docking studies

In order to investigate the most stable conformation suitable for the activation of each receptor, selected top-ranked time-frames (pose conformations) generated from each MD run with the respective homology modeled hNTS1R (400 ns) and hNTS2R (800 ns) were then subjected to molecular docking experiments using SeeSAR (SeeSAR package, Version 13.1 from BioSolveIT GmbH, St. Augustin, 2024) as described in our previously studies (Tzvetkov et al., 2017; Tzvetkov et al., 2019). Based on MD simulations post-analysis of the whole-time interval of MD trajectories, four time-frames for hNTS1R (at 1.0, 3.0, 11, and 393 ns) and four time-frames for hNTS2R (at 1.0, 7.0, 22, and 400 ns) were selected for docking experiments with SeeSAR. The respective conformations of hNTS1R and hNTS2R binding sites were generated using the appropriate Protein, Protein editor, and Binding site modules in SeeSAR. After definition of the binding site within the extracellular part of each receptor, an unconstrained docking step was performed with energetically optimized poses (obtained from previous 2D-NMR analyses) of peptides **3** and **6** used as PDB input structures in SeeSAR (Kühl et al., 2023). The 3D structure of each peptide was then systematically processed within the docking and re-docking steps by applying the Docking module integrated in SeeSAR, which embeds the FlexX/-SIS algorithms as previously described (Tzvetkov et al., 2017; Tzvetkov et al., 2019). The docking experiments in SeeSAR resulted in the generation of a maximum of 10 poses for each peptide in complex with the respective receptor's conformation, which were then post-processed with the HYdrogen DEsolvation (HYDE) algorithm, as implemented in SeeSAR. The docking engine in SeeSAR processed docking modes and poses of a ligand as a function of the empirical docking score, and, after an appropriate post-optimization procedure, also of a HYDE-based computation (Kühl et al., 2023; White et al., 2012). After visual inspection, the best-scored HYDE docking poses of each receptor–ligand complex were selected and further optimized in the next post-scoring step within the binding site of each receptor's conformation in order to increase the scoring probability and stability of the respective protein–ligand complex. This post-scoring step includes a stepwise semi-manual conformational optimization of each ligand in terms of (i) torsions/bindings, (ii) intra-, and (iii) intermolecular clashes by using the integrated in SeeSAR modules Molecular editor, Similarity scanner, and Inspirator. The resulting optimized conformations for each peptide within the binding site of the respective protein–peptide complexes were then subjected to perform successive re-docking and re-scoring steps. In addition, the representative best-scored poses (conformations) of peptides **3** and **6** within each receptor's conformation were visually inspected with the Analyzer module in SeeSAR and saved in SD format and PDB data files for further computations herein.

4.6.6. Post-analysis of molecular docking data

The scoring function of HYDE is used to rapidly estimate the overall binding affinities (the Gibbs free energy of binding, ΔG) of the respective ligand by considering the partial sum of the hydrogen bonds (ΔH) and the dehydration energies (–TΔS) of all non-hydrogen atoms for both, protein and ligand within the respective protein–ligand complex (Reulecke et al., 2008; Schneider et al., 2012). Using a 3D interface, SeeSAR enables to visualize the (HYDE-) estimated ΔG in form of translucent spheres coloring (HYDE "coronas", ranking from dark red (very unfavorable) to dark green (very favorable for binding affinity), with different sizes correlating with the sum of contribution of each non-hydrogen atom within the active site of the respective protein–ligand complex. Consequently, HYDE calculates the predicted binding affinity of each ligand, represented herein as $K_{i\ HYDE}$ ranges and therefore used to calculate the mean $\overline{K}_{i\ HYDE}$ and pK_i values, and also to compute some physicochemical and drug-like properties including logP and ligand-lipophilicity efficiency (LLE). In addition, the obtained best-ranked docking poses for each ligand were visually inspected using the integrated in SeeSAR statistical significance of torsion patterns based on

statistics of occurrence of substructure dihedral deposited in the Cambridge Structural Database (CSD) (Schärfer et al., 2013; Schärfer et al., 2013) As a result, statistically relevant torsions for binding affinity of a certain ligand's conformation were represented with the respective coloring scheme from deep red (rarely/not observed) and orange (observed frequently) to deep green (observed often) torsions (Kühl et al., 2023).

4.6.7. *Visualization of protein–ligand interactions*

The best-predicted docking solutions for peptide **3** and **6** were investigated for their interaction within the active site of the respective hNTS1 or hNTS2 receptor using Biovia Discovery Studio Visualizer 2024 (Dassault Systemes: Vélizy-Villacoublay, France, https://www.3ds.com/).

4.7. *Statistical analysis*

Data are expressed as the mean ± standard deviation (±SD). Statistical analysis and graphs from *in vitro* experiments and MD simulations were performed with GraphPad Prism 6.0 software (GraphPad Software, La Jolla, CA, USA).

Funding Sources.

This work was funded by the Bulgarian National Science Fund (BNSF) under research grant KP-06-N59/2 (КП-06-Н59/2).

Declaration of competing interest

The authors declare that they have no known competing financial interests or personal relationships that could have appeared to influence the work reported in this paper.

Acknowledgments

Financial support by the Bulgarian National Science Fund (BNSF, contract number KP-06-N59/2) is gratefully acknowledged.

Appendix A. Supplementary data

Supplementary data to this article can be found online at https://doi.org/10.1016/j.crbiot.2025.100298.

Data availability

Data will be made available on request.

References

Dawson, V.L., Dawson, T.M., 2019. Promising disease-modifying therapies for Parkinson's disease. Sci. Transl. Med., 11 (520), eaba1659.
Romero-Zerbo, S.-Y., Valverde, N., Claros, S., Zamorano-Gonzalez, P., Boraldi, F., Lofaro, F.-D., Lara, E., Pavia, J., Garcia-Fernandez, M., Gago, B., Martin-Montañez, E., 2024. New molecular mechanisms to explain the neuroprotective effects of insulin-like growth factor II in a cellular model of Parkinson's disease. J. Adv. Res., 67, 349–359.
Videira, P.A.Q., Castro-Caldas, M., 2018. Linking glycation and glycosylation with inflammation and mitochondrial dysfunction in Parkinson's disease. Front. Neurosci., 12, 381.
Tzvetkov, N.T., Stammler, H.-G., Hristova, S., Atanasov, A.G., Antonov, L., 2019. (Pyrrolo-pyridin-5-yl)benzamides: BBB permeable monoamine oxidase B inhibitors with neuroprotective effect on cortical neurons. Eur. J. Med. Chem., 162, 793–809.
Naoi, M., Maruyama, W., Shamoto-Nagai, M., Riederer, P., 2024. Toxic interactions between dopamine, α-synuclein, monoamine oxidase, and genes in mitochondria of Parkinson's disease. J. Neural Transm. (vienna) 131 (6), 639–661.
Kakkar, A.K., Dahiya, N., 2015. Management of Parkinson's disease: current and future pharmacology. Eur. J. Pharmacol., 750, 74–81.
Aarsland, D., Creese, B., Politis, M., Chaudhuri, K.R., Ffytche, D.H., Weintraub, D., Ballard, C., 2017. Cognitive decline in Parkinson disease. Nat. Rev. Neurol., 13 (4), 217–231.
Zigmond, J.M., Smeyne, R.J., 2014. Exercise: is it a neuroprotective and if so, how does it work? Parkinsonism Relat. Disord., 20 (Suppl. 1), S123eS127.
Yeung, A.W.K., Georgieva, M.G., Kirilov, K., Balacheva, A.A., Peeva, M.I., Horbańczuk, O.K., Lucarini, M., Durazzo, A., Santini, A., Souto, E.B., Pajapanova, T. I., Millela, L., Atanasov, A.G., Tzvetkov, N.T., 2020. Neurotensins and their therapeutic potential: Research field study. Future Med. Chem., 12 (19), 1779–1803.
Iyer, M.R., Kunos, G., 2021. Therapeutic approaches targeting the neurotensin receptors. Expert Opin. Ther. Pat., 31 (5), 361–386.
Woodworth, H.L., Perez-Bonilla, P.A., Beekly, B.G., Lewis, T.J., Leinninger, G.M., 2018. Identification of neurotensin receptor expressing cells in the ventral tegmental area across the lifespan. eNeuro 5 (1), e0191–e01917.
Boules, M., Li, Z., Smith, K., Fredrickson, P., Richelson, E., 2013. Diverse roles of neurotensin agonists in the central nervous system. Front. Endocrinol. (lausanne) 4, 36.
Sarret, P., Cavelier, F. (2017). Neurotensin and its receptors, in: Reference module in neuroscience and biobehavioral psychology. Elsevier, pp 1–17.
Tanganelli, S., Antonelli, T., Tomasini, M.C., Beggiato, S., Fuxe, K., Ferraro, L., 2012. Relevance of dopamine D_2/neurotensin NTS1 and NMDA/neurotensin NTS1 receptor interaction in psychiatric and neurodegenerative disorders. Curr. Med. Chem., 19 (3), 304–316.
Plach, M., Schäfer, T., Borroto-Escuela, D.O., Weikert, D., Gmeiner, P., Fuxe, K., Friedland, K., 2019. Differential allosteric modulation within dopamine D_2R-neurotensin NTS1R and D_2R-serotonini 5-HT_{2A}R receptor complexes gives bias to intracellular calcium signalling. Sci. Rep., 9, 16312.
Vincent, J.-P., Mazella, J., Kitabgi, P., 1999. Neurotensin and neurotensin receptors. Trends Pharmacol. Sci., 20 (7), 302–309.
Chartier, M., Desgagné, M., Sousbie, M., Rumsby, C., Chevillard, L., Théroux, L., Haroune, L., Côte, J., Longpré, J.-M., Boundreault, P.-L., Marsault, E., Sarret, P., 2021. Pharmacodynamic and pharmacokinetic profiles of a neurotensin receptor type 2 (NTS2) analgesic macrocyclic analog. Biomed. Pharmacother., 141, 111861.
Sousbie, M., Vivancos, M., Brouillette, R.L., Besserer-Offroy, È., Longpré, J.-M., Leduc, R., Sarret, P., Marsault, È., 2018. Structural optimization and characterization of potent analgesic macrocyclic analogues of neurotensin (8-13). J. Med. Chem., 61 (16), 7103–7115.
Jacobsen, L., Madsen, P., Jacobsen, C., Nielsen, M.S., Gliemann, J., Petersen, C.M., 2001. Activation and functional characterization of the mosaic receptor SorLA/LR11. J. Biol. Chem., 276 (25), 22788–22796.
Li, J.H., Sicard, F., Salam, M.A., Baek, M., LePrince, J., Vaudry, H., Kim, K., Kwon, H.B., Seong, J.Y., 2005. Molecular cloning and functional characterization of a type-I neurotensin receptor (NTR) and a novel NTR from the bullfrog brain. J. Mol. Endocrinol., 34 (3), 793–807.
Kleczkowska, P., Lipkowski, A.W., 2013. Neurotensin and neurotensin receptors: Characteristic, structure-activity relationship and pain modulation – A review. Eur. J. Pharmacol., 716 (1–3), 54–60.
St-Gelais, F., Legault, M., Bourque, M.-J., Rompré, P.-P., Trudeau, L.-E., 2004. Role of calcium in neurotensin-evoked enhancement in firing in mesencephalic dopamine neurons. J. Neurosci., 24 (10), 2566–2574.
Mustain, W.C., Rychahou, P.G., Evers, B.M., 2011. The role of neurotensin in physiologic and pathologic processes. Curr. Opin. Endocrinol. Diabetes Obes., 18 (1), 75–82.
Cáceda, R., Kinkead, B., Nemeroff, C.B., 2006. Neurotensin: role in psychiatric and neurological diseases. Peptides 27 (10), 2385–2404.
Lazarova, M., Popatanasov, A., Klissurov, R., Stoeva, S., Pajpanova, T., Kalfin, R., Tancheva, L., 2018. Preventive effect of two new neurotensin analogues on Parkinsońs disease rat model. J. Mol. Neurosci., 66 (4), 552–560.
Boules, M., Warrington, L., Fauq, A., McCormick, D., Richelson, E., 2001. Antiparkinson-like effects of a novel neurotensin analog in unilaterally 6-hydroxydopamine lesioned rats. Eur. J. Pharmacol., 428 (2), 227–233.
Kühl, T., Georgieva, M.G., Hübner, H., Lazarova, M., Vogel, M., Haas, B., Peeva, M.I., Balacheva, A.A., Bogdanov, I.P., Milella, L., Ponticelli, M., Garev, T., Faraone, I., Detcheva, R., Minchev, B., Petkova-Kirova, P., Tancheva, L., Kalfin, R., Atanasov, A. G., Antonov, L., Pajpanova, T.I., Kirilov, K., Gastreich, M., Gmeiner, P., Imhof, D., Tzvetkov, N.T., 2023. Neurotensin(8-13) analogs as dual NTS1 and NTS2 receptor ligands with enhanced effects on a mouse model of Parkinson's disease. Eur. J. Med. Chem., 254, 115386.
Carraway, R., Leeman, S.E., 1975. The amino acid sequence of a hypothalamic peptide, neurotensin. J. Biol. Chem., 250 (5), 1907–1911.
Sefler, A.M., He, J.X., Sawyer, T.K., Holub, K.E., Omecinsky, D.O., Reily, M.D., Thanabal, V., Akunne, H.C., Cody, W.L., 1995. Design and structure-activity relationships of C-terminal cyclic neurotensin fragment analogues. J. Med. Chem. 38 (2), 249–257.
Keller, M., Kuhn, K.K., Einsiedel, J., Hübner, H., Biselli, S., Mollereau, C., Wifling, D., Svobodova, J., Bernhardt, G., Cabrele, C., Venderheyden, P.M.L., Gmeiner, P., Buschauer, A., 2016. Mimicking of arginine by functionalized N^{ω}-carbamoylated arginine as a new broadly applicable approach to labeled bioactive peptides: High affinity angiotensin, neuropeptide Y, neuropeptide FF, and neurotensin receptor ligands as examples. J. Med. Chem., 59 (5), 1925–1945.
Fanelli, R., Floquet, N., Besserer-Offroy, É., Delort, B., Vivancos, M., Longpré, J.-M., Renault, P., Martinez, J., Sarret, P., Cavelier, F., 2017. Use of molecular modeling to design selective NTS2 neurotensin analogues. J. Med. Chem., 60 (8), 3303–3313.
Schindler, L., Bernhardt, G., Keller, M., 2019. Modifications at Arg and Ile give neurotensin(8-13) derivatives with high stability and retained NTS1 receptor affinity. ACS Med. Chem. Lett., 10 (6), 960–965.
Keller, M., Mahuroof, S.A., Yee, V.H., Carpenter, J., Schindler, L., Littmann, T., Pegoli, A., Hübner, H., Bernhardt, G., Gmeiner, P., Holliday, N.D., 2019. Fluorescence labeling of neurotensin(8-13) via arginine residues gives molecular tools with high receptor affinity. ACS Med. Chem. Lett., 11 (1), 16–22.
Thomas, J.B., Giddings, A.M., Wiethe, R.W., Olepu, S., Warner, K.R., Sarret, P., Gendron, L., Longpre, J.-M., Zhang, Y., Runyon, S.P., Gilmour, B.P., 2014. Identification of *N*-[(5-{[(4-methylphenyl)sulfonyl]amino}-3-(trifluoroacetyl)-1*H*-

indol-1-yl)acetyl]-*L*-leucine (NTRC-824), a neurotensin-like nonpeptide compound selective for the neurotensin receptor type 2. J. Med. Chem., 57, 7472–7477.
Kitabgi, P., De Nadai, F., Rovére, C., Bidard, J.N., 1992. Biosynthesis, maturation, release, and degradation of neurotensin and neuromedin N. Ann. n. y. Acad. Sci. 668, 30–42.
Chartier, M., Desgagné, M., Sousbie, M., Côté, J., Longpré, J.-M., Marsault, E., Sarret, P., 2021. Design, structural optimization, and characterization of the first selective macrocyclic neurotensin receptor type 2 non-opioid analgesic. J. Med. Chem., 64 (4), 2110–2124.
Dubuc, I., Sarret, P., Labbé-Jullié, C., Botto, J.-M., Honoré, E., Bourdel, E., Martinez, J., Costentin, J., Vincent, J.-P., Kitabgi, P., Mazella, J., 1999. Identification of the receptor subtype involved in the analgesic effect of neurotensin. J. Neurosci., 19 (1), 503–510.
White, J.F., Noinaj, N., Shibata, Y., Love, J., Kloos, B., Xu, F., Gvozdenovic-Jeremic, J., Shah, P., Shiloach, J., Tate, C.G., Grisshammer, R., 2012. Structure of the agonist-bound neurotensin receptor. Nature 490 (7421), 508–513.
Tzvetkov, N.T., Stammler, H.-G., Neumann, B., Hristova, S., Antonov, L., Gastreich, M., 2017. Crystal structures, binding interactions, and ADME evaluation of brain penetrant N-substituted indazole-5-carboxamides as subnanomolar, selective monoamine oxidase B and dual MAO-A/B inhibitors. Eur. J. Med. Chem., 127, 470–492.
Tzvetkov, N.T., Antonov, L., 2017. Subnanomolar indazole-5-carboxamide inhibitors of monoamine oxidase B (MAO-B) continued: indications of iron binding, experimental evidence for optimized solubility and brain penetration. J. Enz. Inh. Med. Chem., 32, 960–967.
Chen, X., Murawski, A., Patel, K., Crespi, C.L., Balimane, P.V., 2008. A novel design of artificial membrane for improving the PAMPA model. Pharm. Res., 25 (7), 1511–1520.
Di, L., Kerns, E.H., Fan, K., McConnell, O.J., Carter, G.T., 2003. High throughput artificial membrane permeability assay for blood-brain barrier. Eur. J. Med. Chem., 38 (3), 223–232.
SeeSAR package, Version 13.1 from BioSolveIT GmbH, St. Augustin, 2024, Germany, http://www.biosolveit.de/SeeSAR.
Reulecke, I., Lange, G., Albrecht, J., Klein, R., Rarey, M., 2008. Towards an integrated description of hydrogen bonding and dehydration: decreasing false positives in virtual screening with the HYDE scoring function. ChemMedChem 3 (6), 885–897.
Schneider, N., Hindle, S., Lange, G., Klein, R., Albrecht, J., Briem, H., Beyer, K., Claußen, H., Gastreich, M., Lemmen, C., Rarey, M., 2012. Substantial improvements in large-scale redocking and screening using the novel HYDE scoring function. J. Comput. Aided Mol. Des., 26 (6), 701–723 and references therein.
Schärfer, C., Schulz-Gasch, T., Hert, J., Heinzerling, L., Schulz, B., Inhester, T., Stahl, M., Rarey, M., 2013. CONFECT: conformations from an expert collection of torsion patterns. ChemMedChem 8 (10), 1690–1700.
Schärfer, C., Schulz-Gasch, T., Ehrlich, H.-C., Guba, W., Rarey, M., Stahl, M., 2013. Torsion angle preferences in drug-like chemical space: a comprehensive guide. J. Med. Chem., 56 (5), 2016–2028.
Kato, H.E., Zhang, Y., Hu, H., Suomivuori, C.-M., Kadji, F.M.N., Aoki, J., Kumar, K.K., Fonseca, R., Hilger, D., Huang, W., Latorraca, N.R., Inoue, A., Dror, R.O., Kobilka, B. K., Skiniotis, G., 2019. Conformational transitions of a neurotensin receptor 1 – Gi1 complex. Nature 572 (7767), 80–85.
Kühl, T., Wißbrock, A., Goradia, N., Sahoo, N., Galler, K., Neugebauer, U., Popp, J., Heinemann, S.H., Ohlenschläger, O., Imhof, D., 2013. Analysis of Fe(III) heme binding to cysteine-containing heme-regulatory motifs in proteins. ACS Chem. Biol., 8, 1785–1793.
Brewitz, H.H., Kühl, T., Goradia, N., Galler, K., Popp, J., Neugebauer, U., Ohlenschläger, O., Imhof, D., 2015. Role of the chemical environment beyond the coordination site: structural insight into Fe(III) protoporphyrin binding to cysteine-based heme-regulatory protein motifs. ChemBioChem 16 (15), 2216–2224.
Heimer, P., Tietze, A.A., Baüml, C.A., Resemann, A., Mayer, F.J., Suckau, D., Ohlenschläger, O., Tietze, D., Imhof, D., 2018. Conformational μ-conotoxin PIIIA isomers revisited: impact of cysteine pairing on disulfide-bond assignment and structure elucidation. Anal. Chem., 90 (5), 3321–3327.
Studer, G., Rempfer, C., Waterhouse, A.M., Gumienny, R., Haas, J., Schwede, T., 2020. QMEANDisCo-distance constraints applied on model quality estimation. Bioinformatics 36 (6), 1765–1771.
Roberts, E., Eargle, J., Wright, D., Luthey-Schulten, Z., 2006. MultiSeq: unifying sequence and structure data for evolutionary analysis. BMC Bioinformatics 7, 382.
Tzvetkov, N.T., Stammler, H.-G., Georgieva, M.G., Russo, D., Faraone, I., Balacheva, A. A., Hristova, S., Atanasov, A.G., Milella, L., Antonov, L., Gastreich, M., 2019. Carboxamides vs. methanimines: crystal structures, binding interactions, photophysical studies, and biological evaluation of (indazole-5-yl)methanimines as monoamine oxidase B and acetylcholinesterase inhibitors. Eur. J. Med. Chem., 179, 404–422.